Journal of Materials Chemistry A

ROYAL SOCIETY OF CHEMISTRY

PAPER

View Article Online
View Journal | View Issue

Cite this: J. Mater. Chem. A, 2021, 9, 2850

A robust heterometallic ultramicroporous MOF with ultrahigh selectivity for propyne/propylene separation†

Yun-Lei Peng, ‡[ab] Ting Wang,‡[a] Chaonan Jin,[d] Pengfei Li,[a] Shanelle Suepaul,[e] Gary Beemer,[f] Yao Chen, [d] Rajamani Krishna, [g] Peng Cheng, [ac] Tony Pham, [ef] Brian Space, [e] Michael J. Zaworotko [b] and Zhenjie Zhang *[acd]

Received 30th August 2020
Accepted 15th December 2020

DOI: 10.1039/d0ta08498k

rsc.li/materials-a

Highly efficient removal of trace propyne (C_3H_4) (propyne <1000 ppm) from propylene (C_3H_6) is an essential and challenging industrial process due to the high molecular similarity of C_3H_4 and C_3H_6. Herein, we created a new ultramicroporous metal–organic framework (NKMOF-11) with exceptional water stability, superior C_3H_4 binding affinity, and ultrahigh uptake capacity of C_3H_4 at ultra-low pressure (0.1 mbar). Modelling studies revealed that the excellent performance of NKMOF-11 can be attributed to the suitable pore aperture and unique binding sites for C_3H_4 through strong hydrogen bonding and π–π interactions. Attributed to the preferred adsorption of C_3H_4, NKMOF-11 possessed ultrahigh selectivities towards C_3H_4/C_3H_6 mixtures (1/99 and 1/999 (v/v)) at room temperature. The simulation and experimental breakthrough results further revealed that NKMOF-11 possesses excellent separation performance towards C_3H_4 and C_3H_6 binary mixtures (1/99 and 1/999) and sets a new record for the productivity of polymer-grade C_3H_6 (>99.996%) among all reported materials. This study paves a new avenue for the design of adsorbent materials with both high selectivity and high productivity for a C_3H_4/C_3H_6 binary mixture.

Introduction

Propylene (C_3H_6) is a relevant industrial raw material widely used as essential building blocks for the production of polypropylene, propylene oxide, and acrylonitrile. The worldwide production capacity of propylene was up to 120 million tons in 2017, only lower than that of ethylene.[1] C_3H_6 is mainly produced through the cracking of naphtha or the fractional distillation of hydrocarbons, which inevitably introduces a trace amount of propyne (C_3H_4) as impurities. The C_3H_4 impurity will severely affect the downstream application of propylene, *e.g.*, poisoning the polymerization catalyst of C_3H_6.[2] Therefore, to meet the requirements for propylene polymerization, the C_3H_4 content must be reduced to 40 ppm or less.[3] Currently, selective hydrogenation using noble metal catalysts is a widely used technique to remove trace amounts of C_3H_4. However, these techniques face some deficiencies such as high cost, short catalyst lifetime, low efficiency, and possible secondary pollution.[4] Therefore, it is urgent and significant to develop some new techniques and materials for efficient removal of trace C_3H_4 from C_3H_6.

Recently, a simple and efficient alternative has emerged to selectively adsorb C_3H_4 over C_3H_6 using porous materials as physisorbents.[5] Metal–organic frameworks (MOFs) (sometimes referred to as porous coordination polymers, PCPs) are a new class of porous materials that have demonstrated great potential for gas separation applications, due to their well-defined structure, ultra-high specific surface area (>7300 $m^2\ g^{-1}$), fine-tunable pore size, customizable functional groups, and facile post-synthesis.[6–8] Hitherto, much exciting progress in MOFs has been made for the separation of propyne/propylene,[9] acetylene/ethylene,[10–14] ethylene/ethane,[15,16] carbon dioxide/methane,[17–19] carbon dioxide/nitrogen,[20–23] acetylene/carbon dioxide[24,25] and noble gases.[26] However, separation of C_3H_4/C_3H_6 using MOFs is still underexplored but of great significance. The challenge to

[a]College of Chemistry, Nankai University, Tianjin, 300071, P. R. China. E-mail: zhangzhenjie@nankai.edu.cn

[b]Department of Chemical Sciences, Bernal Institute, University of Limerick, Limerick, V94T9PX, Republic of Ireland

[c]Key Laboratory of Advanced Energy Materials Chemistry (MOE), Nankai University, Tianjin 300071, China

[d]State Key Laboratory of Medicinal Chemical Biology, Nankai University, Tianjin 300071, China

[e]Department of Chemistry, University of South Florida, 4202 East Fowler Avenue, CHE205, Tampa, Florida 33620-5250, USA

[f]Department of Chemistry, Biochemistry and Physics, The University of Tampa, 401 West Kennedy Boulevard, Tampa, Florida 33606-1490, USA

[g]Van't Hoff Institute for Molecular Sciences, University of Amsterdam, Science Park 904, 1098 XH, Amsterdam, The Netherlands

† Electronic supplementary information (ESI) available. See DOI: 10.1039/d0ta08498k

‡ These authors contributed equally to this work.

separate C_3H_4/C_3H_6 could be attributed to the following considerations. (i) Their similar molecular structure and size (C_3H_4: 4.16 × 4.01 × 6.51 Å^3, C_3H_6: 5.25 × 4.16 × 6.44 Å^3) require precise tuning of the pore aperture of adsorbents (in 1 Å scale increment) to separate C_3H_4/C_3H_6 (Scheme 1); (ii) the majority of reported MOFs lack binding sites with specific affinity for C_3H_4. The specific binding sites between C_3H_4 with frameworks reported in the literature include open metal sites, hydrogen bonding interaction, π–π interaction and inorganic anions such as SiF_6^{2-}, TiF_6^{2-}, and $NbOF_5^{2-}$. Exploring new types of functional sites with strong C_3H_4 binding affinity is essential for the development of new MOF materials for the C_3H_4/C_3H_6 separation application.

Herein, we constructed a new robust ultramicroporous MOF, NKMOF-11, with an exceptional binding affinity to C_3H_4. The modeling study revealed that the outstanding performance of NKMOF-11 could be ascribed to the precisely tuned pore aperture and strong specific binding sites for C_3H_4 from pyrazine and thiol groups. Moreover, NKMOF-11 offered ultrahigh selectivity for C_3H_4/C_3H_6 (1/99 and 1/999), verified using both ideal adsorbed solution theory (IAST) calculations,[27] and simulated/experimental breakthrough data.

Experimental section

Materials

All chemicals were used as received without further purification.

Synthesis of NKMOF-11

NKMOF-11 was produced using the following approach. NiI_2 (0.2170 g, 0.001125 mol) was dissolved in acetonitrile (30 mL) by sonication and stirred for two days. $Na[Cu(pdt)_2]\cdot 2H_2O$ (0.30 g, 0.00075 mol) was dissolved in acetonitrile (200 mL) and bubbled with argon for 1 hour. Subsequently, NiI_2 solution was dropwise added into $Na[Cu(pdt)_2]\cdot 2H_2O$ solution. After 2 hours, dark powders of NKMOF-11 were obtained by centrifugation. The raw produce was washed using a Soxhlet extractor for 24 hours. The purity of the bulky sample was verified by PXRD.

Single-component gas sorption measurement

200–250 mg of NKMOF-11 was prepared to test single component gas adsorption. NKMOF-11 was activated at 90 °C for 10 h under dynamic pressure below 5 μmHg. Single-component gas sorption isotherms were measured at 273 K, 298 K, 308 K, and 318 K using an ASAP 2020 Plus Analyzer (Micromeritics).

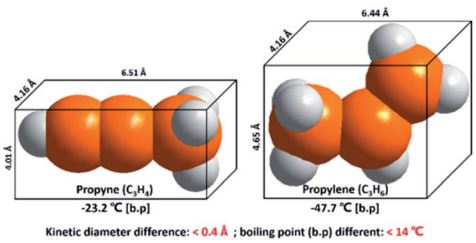

Scheme 1 Molecular structure and physical properties of propyne and propylene (b.p. = boiling point).

Breakthrough experiment

The breakthrough experiments for C_3H_4/C_3H_6 (1/99 v/v) and C_3H_4/C_3H_6 (1/999 v/v) mixtures were carried out at a flow rate of 2 mL min^{-1} (298 K, 1.01 bar). Activated MOF (about 0.2 g for each test) powders were packed into a d.p. 4 × 100 mm stainless steel column under a pure He atmosphere. The samples in the column were compressed under the same conditions, and the column voidages were similar for different samples in order to compare the separation performance. The experimental set-up consisted of two fixed-bed stainless steel reactors. One reactor was loaded with the adsorbent, while the other reactor was used as a blank control group to stabilize the gas flow. The horizontal reactors were placed in a temperature-controlled environment maintained at 298 K. The flow rates of all gas mixtures were regulated using mass flow controllers, and the effluent gas stream from the column was monitored by gas chromatography (FID-Flame Ionization Detector, detection limit 100 ppb). Prior to the breakthrough experiment, we activated the sample by flushing the adsorption bed with helium gas for 30 min at 323 K. Before each separation test, the adsorption bed was regenerated using a He flow (40 mL min^{-1}) for 12 h at 363 K to ensure the complete removal of the adsorbed gas.

The C_3H_6 productivity (q) is defined by the breakthrough amount of C_3H_6, which is calculated by integration of the breakthrough curves $f(t)$ during a period from t_1 to t_2 where the C_3H_6 purity is higher than or equal to a threshold value p:

$$q = \frac{C_i(C_3H_6)}{C_i(C_3H_6) + C_i(C_3H_4)} \times \left(\int_{t_1}^{t_2} f(t)\mathrm{d}t \right)$$

Fourier infrared spectroscopy

All tests were carried out in a glove box. For C_3H_4@NKMOF-11, the sample was pre-filled with a propyne balloon for 4 hours, and then quickly transferred to the glove box. For 1% C_3H_4@NKMOF-11 and 0.1% C_3H_4@NKMOF-11, the sample was pre-filled with a C_3H_4/C_3H_6 (1/99 and 1/999 (v/v)) mixed gas balloon for 4 hours, and then quickly transferred to the glove box for testing.

Results and discussion

NKMOF-11 was prepared *via* a reaction of NiI_2 with a metalloligand of $Na[Cu(pdt)_2]$ (pdt = pyrazine-2,3-dithiol). After thorough washing with acetonitrile, we obtained a black powder product with a particle size of 100 nm (Fig. S1†). Moreover, the powder X-ray diffraction (PXRD) result matched well with the structure of NKMOF-1-M (M = Cu or Ni) reported previously (Fig. 1).[1b] This result indicated that we successfully obtained a new MOF isostructural to NKMOF-1-M (Fig. S2†). Elemental analysis, EDX (energy-dispersive X-ray spectroscopy) and ICP-OES (inductively coupled plasma-optical emission spectrometry) results (Fig. S3†) showed that NKMOF-11 possesses

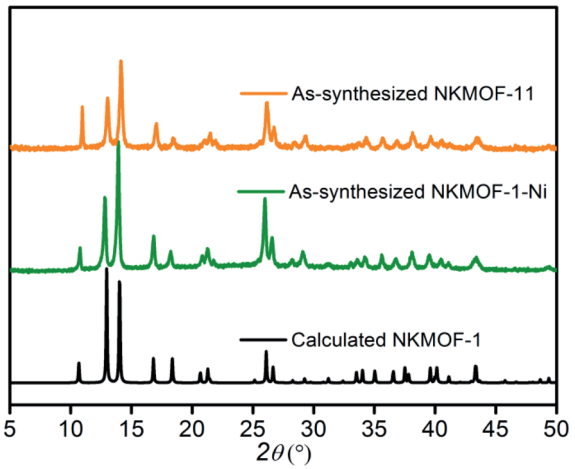

Fig. 1 The experimental PXRD patterns of NKMOF-11 and NKMOF-1-Ni compared with the calculated pattern of NKMOF-1.

a molecular formula of Ni[Cu(pdt)$_2$], in which the ratio of Cu to Ni is 1 to 1. Furthermore, it is worth pointing out NKMOF-11 possesses a different sample color and UV-Vis spectrum to NKMOF-1-Ni (Fig. S2†), indicating the existence of structural differences. In NKMOF-11, the planar [Cu(pdt)$_2$] building blocks were connected by four 4-coordinated Ni cations with square planar geometry to form a three-dimensional (3D) network of pts topology, which possesses one-dimensional (1D) square channels with a pore size around 5.7 Å (after subtracting the van der Waals radius) along the *c* direction (Fig. 2). Moreover, both the conjugated pyrazine rings and metal centers (Cu) located on the wall of the 1D channels can potentially serve as distinct binding sites for gas molecules. N_2 sorption data collected at 77 K revealed that NKMOF-11 possessed a surface area of 376 m^2 g^{-1}. The pore size distribution is mainly concentrated around ~5.3 Å (Fig. S4†), consistent with the structural measurement (Fig. 2c). Water stability is an essential factor for MOF materials in real industrial applications. NKMOF-11 can still retain its crystallinity and porosity after soaking in water for >2 years, or at pH = 1 and 12 for one week, verified by PXRD (Fig. S5†) and BET surface area measurements (Fig. S6†).

Single-component gas adsorption data for C_3H_4 and C_3H_6 were collected for NKMOF-11 at different temperatures to explore their potential for C_3H_4/C_3H_6 separation (Fig. 2 and S7†). We found that NKMOF-11 can adsorb 3.1 mmol g^{-1} of C_3H_4, which is much higher than the uptake of C_3H_6 (1.5 mmol g^{-1}) at 1.0 bar and 298 K. It is noteworthy that the C_3H_4 adsorption of NKMOF-11 exhibited type I adsorption isotherms with steep curves in the low-pressure region at all tested temperatures (273 K, 298 K, 308 K and 318 K), indicative of its remarkably strong binding affinity to C_3H_4. Gas adsorption selectivity is usually closely related to the adsorption behavior in the low-pressure region. Thus, we further analyzed the adsorption behaviors for each gas (C_3H_4 and C_3H_6) in the low-pressure region at 298 K. The C_3H_4 uptake capacity of NKMOF-11 can

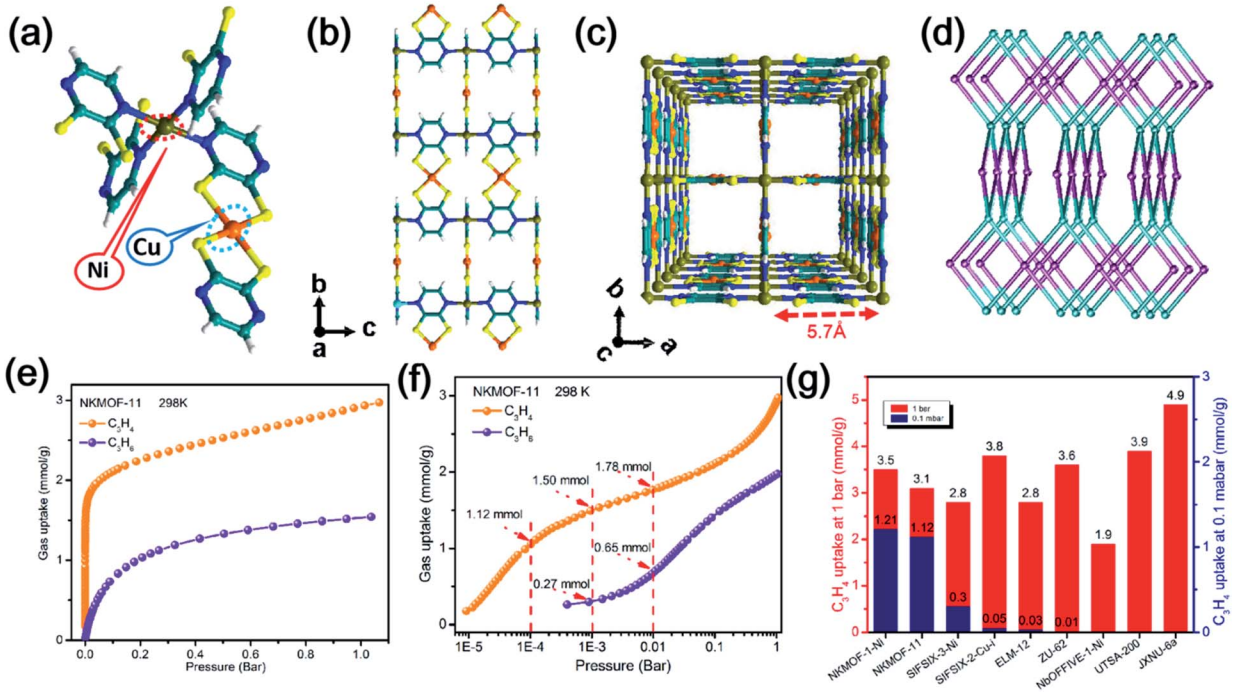

Fig. 2 Coordination environment, 3D structure, and topology. (a) The coordination environment of metals in NKMOF-11. (b) The 3D structure of NKMOF-11 viewed along the *a* axis. (c) The 3D structure of NKMOF-11 viewed along the *c* axis. (d) Illustration of the pts topology of NKMOF-11 (violet node for Ni and teal node for the metalloligand). (e) Single-component (C_3H_4 and C_3H_6) gas adsorption isotherms of NKMOF-11 at 298 K (0–1 bar). (f) Log scale of single-component (C_3H_4 and C_3H_6) gas adsorption isotherms of NKMOF-11 at 298 K (0–1 bar). (g) Comparison of some state-of-the-art materials for C_3H_4 uptake at 1 bar and 0.1 mbar (298 K). Atom colors: C = teal, H = white, N = blue, S = yellow, Cu = orange, and Ni = dark yellow.

achieve 1.78 and 1.50 mmol under 0.01 and 0.001 bar, respectively, while the uptake capacity of C_3H_6 is fairly low (0.65 and 0.27 mmol, respectively) (Fig. 2f). At ultra-low pressure (0.1 mbar), the C_3H_4 uptake capacity of NKMOF-11 reached a remarkably high value of 1.12 mmol g^{-1}, only lower than that of the benchmark material, NKMOF-1-Ni (1.21 mmol g^{-1}) (Fig. 2f and g).[26] This unusual adsorption behavior of C_3H_4 in the ultra-low-pressure region indicated a strong C_3H_4–sorbent interaction. Meanwhile, the uptake capacity of C_3H_6 is almost non-detectable for NKMOF-11 at 0.1 mbar (Fig. 2f). These results indicate the great potential for NKMOF-11 to separate the C_3H_4/C_3H_6 binary mixture.

The isosteric enthalpy of adsorption (Q_{st}) of NKMOF-11 was calculated to estimate the binding affinity of sorbents towards gases quantitatively. Firstly, the adsorption isotherms of single-component gases were fitted with the Dual-Site-Langmuir–Freundlich (DSLF) isotherm model (Tables S1 and S2†). The Q_{st} of C_3H_4 and C_3H_6 was calculated based on the Clausius–Clapeyron equation, which afforded the results of 84.8 kJ mol^{-1} and 30.5 kJ mol^{-1} for NKMOF-11 at zero coverage (Fig. S8†). The big difference of Q_{st} between C_3H_4 and C_3H_6 reveals that NKMOF-11 is a good candidate for C_3H_4/C_3H_6 separation.

To further evaluate the separation performance of adsorbent materials, we calculated the gas mixture selectivity of NKMOF-11 using ideal adsorption solution theory (IAST). As displayed in Fig. 3a and b, the adsorption selectivities of NKMOF-11 for C_3H_4/C_3H_6 mixtures are determined to be 1074 and 1388, for the molar ratio of 1/99 (v/v) and 1/999 (v/v), respectively, at 1 bar. The selectivities of NKMOF-11 for C_3H_4/C_3H gas mixtures (1/99 and 1/999) are just lower than those of the current benchmark material (UTSA-200 with a molecular sieving effect), but higher than those of other state-of-the-art materials, *e.g.*, more than two orders of magnitude better than that of SIFSIX-2-Cu-i (12 for 1/99 (v/v)) and twenty times higher than that of SIFSIX-3-Ni (63 for 1/999 (v/v)).[9a]

Transient breakthrough simulations were performed to compare the productivities of polymer-grade C_3H_6 (content of C_3H_4 < 40 ppm) for NKMOF-11 with the current benchmark materials (SIFISX-3-Ni, SIFSIX-2-Cu-i, ELM-12, and ZU-62) for the separation of 1/99 and 1/999 C_3H_4/C_3H_6 mixtures under industrial conditions. Fig. 3c and d show the outlet concentrations of C_3H_4 exiting the fixed bed of NKMOF-11 as a function of the dimensionless time, τ, at 1 bar and 298 K for 1/99 and 1/999 C_3H_4/C_3H_6 mixtures. Attributed to the record-high C_3H_4/C_3H_6 selectivities of 1/99 and 1/999 C_3H_4/C_3H_6 mixtures, both τ break values for NKMOF-11 are much longer than those of the current benchmark materials. For the hierarchy of τ break values, NKMOF-11 > SIFSIX-3-Ni > ZU-62 > ELM-12 > SIFSIX-2-Cu-i for both different gas ratio mixtures (1/99 and 1/999). Moreover, NKMOF-11 possesses the highest C_3H_6 productivities up to 271.7 mol L^{-1} (1/99, C_3H_4/C_3H_6) and 1404.7 mol L^{-1} (1/999, C_3H_4/C_3H_6), respectively (Table S12†). Normally, the separation performance of adsorbents in the industrial fixed-bed absorber is determined *via* not only gas mixture selectivity but also the productivity of

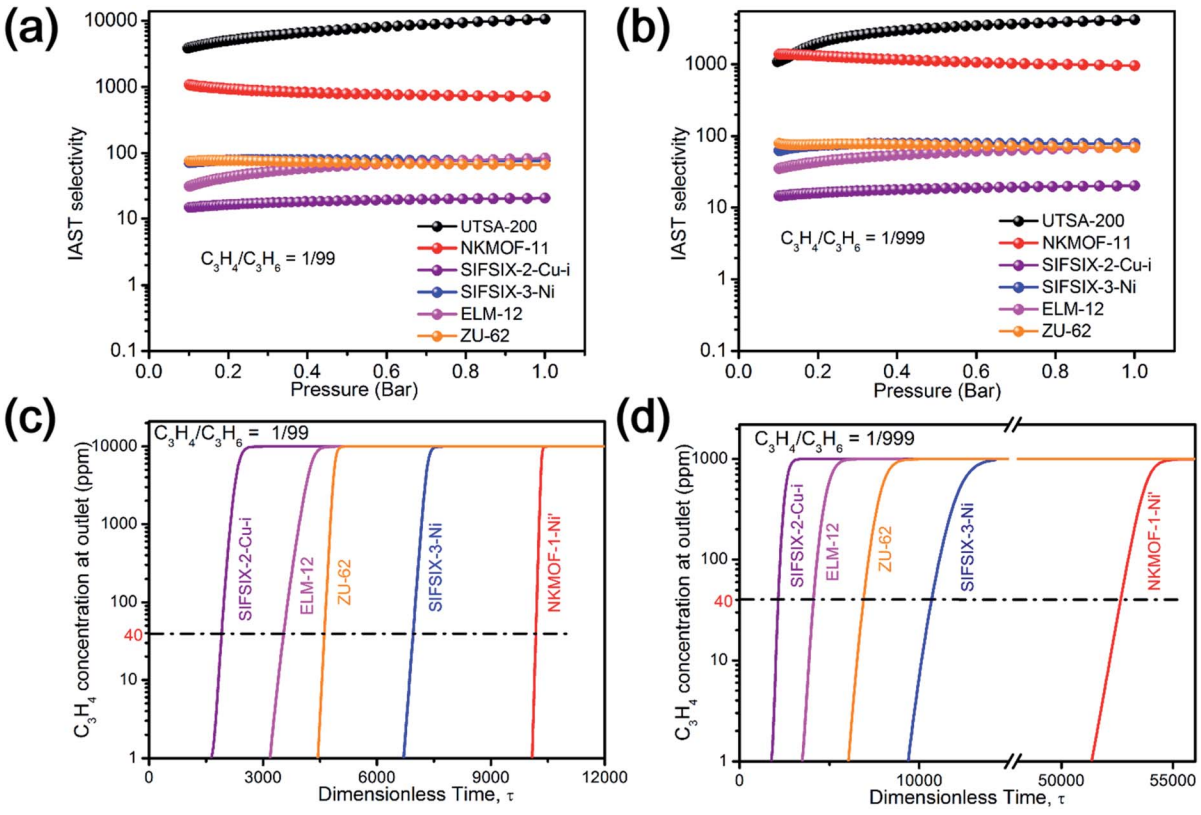

Fig. 3 (a and b) IAST adsorption selectivities of C_3H_4/C_3H_6 for 1/99 and 1/999 at 298 K; (c and d) calculated breakthrough curves for separation of the C_3H_4/C_3H_6 (1/99 and 1/999) mixture at 298 K.

desired gases. Thus, NKMOF-11 demonstrated excellent C_3H_4/C_3H_6 separation performance, which surpasses that of current benchmark materials, and was set as a unique MOF platform to achieve both high selectivity and productivity. These results provide important guidance on using ultramicroporous MOFs as physisorbents to potentially resolve industrial challenges related to C_3H_4/C_3H_6 binary mixture separation.

In order to further establish the feasibility of C_3H_4/C_3H_6 separation on NKMOF-11 under kinetic conditions, gas mixture breakthrough experiments were performed, which are strongly pertinent to the vacuum swing adsorption (VSA) process, an energetically efficient method for industrial-scale separations. Breakthrough experiments were performed on an in-house-constructed separation apparatus (Scheme S1 and Table S6†), in which C_3H_4/C_3H_6 (1/99 and 1/999) mixtures were used as feeds to mimic the industrial process conditions. The result showed that the NKMOF-11 displayed excellent C_3H_4/C_3H_6 mixture separation abilities at 298 K. As shown in Fig. 4a, C_3H_6 was first eluted through the bed, while C_3H_4 was still adsorbed, affording the pure polymer-grade C_3H_6 with no detectable C_3H_4 (detection limit 0.1 ppm). After a certain time, C_3H_4 was eluted from the column and quickly reached equilibrium. The retention time of pure C_3H_6 for the C_3H_4/C_3H_6 (1/99) mixture on NKMOF-11 reached 165 min, significantly higher than that of the current benchmark material, SIFSIX-2-Cu-i, under the same conditions (84 min) (Fig. 4a). Moreover, such excellent C_3H_4/C_3H_6 (1/99) breakthrough performance of NKMOF-11 was closely associated with its ultrahigh C_3H_4/C_3H_6 selectivity at room temperature. The productivity of pure C_3H_6 (C_3H_4 < 1 ppm) obtained from the 1/99 mixture for NKMOF-11 was up to 74.4 mmol per gram (Fig. 4c; Table S7†). In addition, the separation performance of NKMOF-11 for the C_3H_4/C_3H_6 (1/999) mixture was also investigated and compared with that of the benchmark material, SIFSIX-3-Ni (Fig. 4b). Notably, benefitting from the high C_3H_4 uptake and high C_3H_4/C_3H_6 adsorption selectivity in the low-pressure region, NKMOF-11 exhibited remarkable separation ability for the C_3H_4/C_3H_6 (1/999) mixture. The elution time interval for C_3H_6 (362 min) was more than two times longer than that of SIFSIX-3-Ni (177 min). Also, the C_3H_6 productivity of NKMOF-11 (165.1 mmol g^{-1}) calculated from the C_3H_4/C_3H_6 (1/999) breakthrough curve was much higher than that of SIFSIX-3-Ni (69.5 mmol g^{-1}) (Fig. 4c and Table S7†). To investigate the reusability and structural stability on NKMOF-11, cycling breakthrough experiments for the C_3H_4/C_3H_6 (1/99) mixture associated with PXRD were conducted on NKMOF-11 under the same conditions. The breakthrough curves for C_3H_4 and C_3H_6 in five cycles almost overlapped (Fig. 4d), and the crystallinity of NKMOF-11 was retained (Fig. S5†), indicative of the excellent reusability and robustness of NKMOF-11.

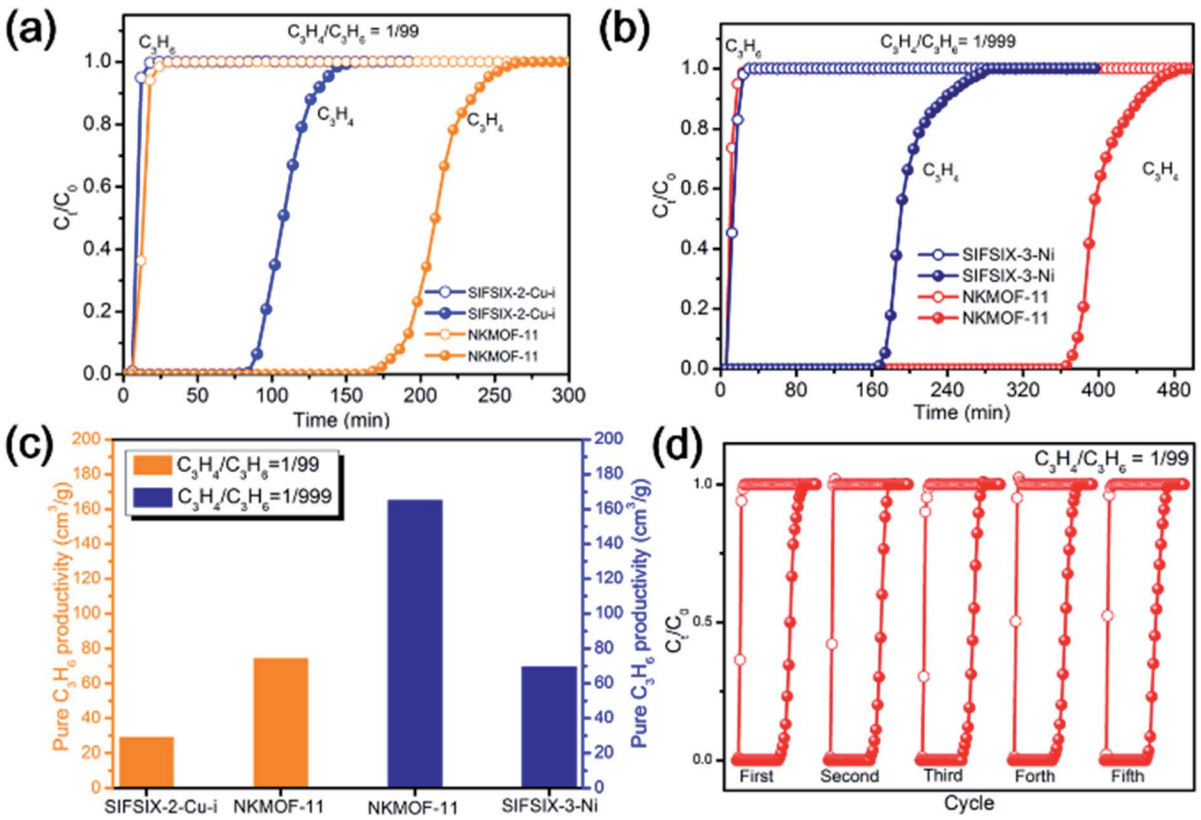

Fig. 4 Experimental column breakthrough curves: (a) C_3H_4/C_3H_6 (1/99); (b) C_3H_4/C_3H_6 (1/999) mixtures on NKMOF-11 *vs.* benchmark materials at 298 K; (c) comparing the productivity of pure C_3H_6 for the corresponding breakthrough experiments with that of benchmark materials reported; (d) cycling tests of NKMOF-11 for the 1/99 C_3H_4/C_3H_6 mixture (sample weight: NKMOF-11, 0.180 g (1/99), 0.185 g (1/999); SIFSIX-2-Cu-i, 0.185 g; SIFSIX-3-Ni, 0.185 g; gas velocity: 2.0 mL min^{-1}).

Grand Canonical Monte Carlo (GCMC) and periodic DFT simulations of C_3H_4 and C_3H_6 adsorption were performed to gain insight into the guest's discriminatory effect for trace C_3H_4 over C_3H_6 in NKMOF-11 and identify the binding sites for these adsorbates in the material. More details for carrying out the GCMC simulations are provided in the ESI (Fig. S9 and Table S8†). The modeled structure at saturation for C_3H_4 and C_3H_6 (Fig. S10 and S11†) revealed that these gases adsorbed at two main binding sites: (1) between the pyrazine units and (2) between the CuS_4 units (denoted sites I and II, respectively). Periodic DFT calculations were performed for a single C_3H_4 and C_3H_6 molecule about both binding sites in NKMOF-11 using the Vienna *ab initio* Simulation Package (VASP).[28,29] Additional details on these calculations are presented in the ESI.† Calculation of the adsorption energy (ΔE) for the optimized position of C_3H_4 and C_3H_6 about site I in NKMOF-11 revealed values of -70.09 and -43.32 kJ mol^{-1}, respectively (Table S9†). These binding energies are comparable to the Q_{st} values at zero coverage for the respective adsorbates (Fig. S8†). The magnitude of the ΔE for C_3H_4 localized at site I is significantly greater than that for C_3H_6 at the same site. The region between the four pyrazine units is highly favorable for C_3H_4, mainly due to strong π–π interactions between the C≡C of the adsorbate and the aromatic rings. In addition, H···S hydrogen bonding interactions occur between the methyl groups of C_3H_4 and the S atoms of the pdt linkers. The HC≡C–CH_3···S interaction distances for the optimized position for C_3H_4 at site I were measured to be 2.80, 2.80, and 2.82 Å (Fig. 5b). On the other hand, it appears that C_3H_6 has a less favorable fit about the four adjacent pyrazine units, due the larger molecular dimensions of this adsorbate compared to C_3H_4. The ΔE values for C_3H_4 and C_3H_6 adsorbed at site II in NKMOF-11 were calculated to be -54.11 and -55.68 kJ mol^{-1}, respectively (Table S9†). In this region, a favorable interaction exists between the negatively charged unsaturated C atoms and the positively charged Cu ions of the CuS_4 units for both adsorbates (Fig. S12†). The binding energy for C_3H_6 at site II is slightly higher than that for C_3H_4, presumably because it possesses more H atoms, which in turn allows it to make more contacts with the framework within this region. Moreover, we also measured the FT-IR spectra for NKMOF-11 treated with C_3H_4/C_3H_6 mixed gas (1/999). The result showed that there were typical C_3H_4 vibration peaks located around 3250 and 612 cm^{-1} (Fig. S13†). However, no signals for C_3H_6 were detected, further validating the high binding affinity of C_3H_4 *vs.* C_3H_6.

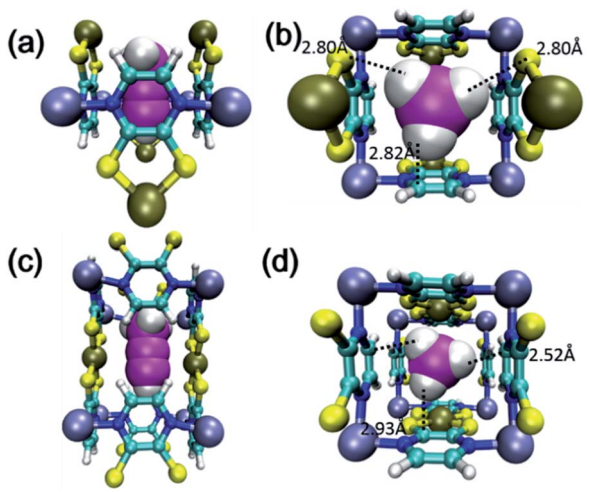

Fig. 5 Perspective views (*a*/*b*-axis, *c*-axis) of a portion of the crystal structure of NKMOF-11 showing the optimized position of propyne molecule about the pyrazine units ((a) *a*/*b*-axis; (b) *c*-axis) and the CuS_4 units ((c) *a*/*b*-axis; (d) *c*-axis) in the MOFs as determined through periodic DFT calculations using the VASP. The closest MOF-adsorbate distances are also shown. Atom colors: C(MOF) = cyan, C(propene) = magenta, H = white, N = blue, S = yellow, Ni = silver, and Cu = gold.

Conclusion

In summary, we reported a new heterometallic ultramicroporous MOF (NKMOF-11) with high robustness, especially outstanding hydrolytic stability. This MOF possessed a 3D pts network with uniform 1D square channels. Single-component gas adsorption data and Q_{st} calculation revealed that NKMOF-11 showed a high affinity to bind with C_3H_4 rather than C_3H_6. Attributed to the selective binding affinity to C_3H_4, the selectivities of NKMOF-11 for 1/99 and 1/999 C_3H_4/C_3H_6 are much higher than those of the benchmark materials, more than two orders of magnitude better than that of SIFSIX-2-Cu-i and twenty times higher than that of SIFSIX-3-Ni. Furthermore, both simulated and experimental gas mixture breakthrough tests proved that NKMOF-11 exhibits excellent separation performance for C_3H_4/C_3H_6 and the highest productivity of polymer-grade purity C_3H_6, which surpass those of current benchmark materials. Modeling studies revealed the occupancy, position, and interactions of C_3H_4 molecules, and revealed that the superior performance of NKMOF-11 could be attributed to the suitable pore aperture and a distinct type of specific binding site for C_3H_4 with strong hydrogen bonding interaction with thiol groups and π–π interactions with pyrazine groups. This work not only provides a new adsorbent material with strong binding affinity for C_3H_4, but also provides important guidance on using ultramicroporous MOFs as physisorbent materials to resolve industrial challenges related to C_3H_4 separation potentially.

Conflicts of interest

There are no conflicts to declare.

Acknowledgements

This work was supported by the National Natural Science Foundation of China (21971126). We also thank Professor Libo Li from Taiyuan University of Technology for the pre-evaluation of the materials' properties.

Notes and references

1 (*a*) L. Li, R.-B. Lin, R. Krishna, X. Wang, B. Li, H. Wu, J. Li, W. Zhou and B. Chen, *J. Am. Chem. Soc.*, 2017, **139**, 7733–

7736; (*b*) Y.-L. Peng, C. He, T. Pham, T. Wang, P. Li, R. Krishna, K. A. Forrest, A. Hogan, S. Suepaul, B. Space, M. Fang, Y. Chen, M. J. Zaworotko, J. Li, L. Li, Z. Zhang, P. Cheng and B. Chen, *Angew. Chem., Int. Ed.*, 2019, **58**, 10209–10214.

2 K. Buckl and A. P. Meiswinkel, *Ullmann's Encyclopedia of Industrial Chemistry*, Wiley VCH Verlag GmbH & Co. KGaA, Weinheim, 2000, pp. 337–340.

3 A. J. McCue, A. Guerrero-Ruiz, I. Rodríguez-Ramos and J. A. Anderson, *J. Catal.*, 2016, **340**, 10–16.

4 D. Teschner, J. Borsodi, A. Wootsch, Z. Révay, M. Hävecker, A. Knop-Gericke, S. D. Jackson and R. Schlögl, *Science*, 2008, **320**, 86–89.

5 (*a*) Z. Bao, G. Chang, H. Xing, R. Krishna, Q. Ren and B. Chen, *Energy Environ. Sci.*, 2016, **9**, 3612–3641; (*b*) R.-B. Lin, S. Xiang, H. Xing, W. Zhou and B. Chen, *Coord. Chem. Rev.*, 2019, **378**, 87–103; (*c*) T. Lan, L. Li, Y. Chen, X. Wang, J. Yang and J. Li, *Mater. Chem. Front.*, 2020, **4**, 1954–1984.

6 Z. Chen, P. Li, R. Anderson, X. Wang, X. Zhang, L. Robison, L. R. Redfern, S. Moribe, T. Islamoglu, D. A. Gómez-Gualdrón, T. Yildirim, J. F. Stoddart and O. K. Farha, *Science*, 2020, **368**, 297–303.

7 (*a*) D. A. Gómez-Gualdrón, P. Z. Moghadam, J. T. Hupp, O. K. Farha and R. Q. Snurr, *J. Am. Chem. Soc.*, 2016, **138**, 215–224; (*b*) P. Li, N. A. Vermeulen, C. D. Malliakas, D. A. Glmez-Gualdrln, A. J. Howarth, B. L. Mehdi, A. Dohnalkova, N. D. Browning, M. O'Keeffe and O. K. Farha, *Science*, 2017, **356**, 624–627.

8 O. Delgado-Friedrichs, S. T. Hyde, M. O'Keeffe and O. M. Yaghi, *Struct. Chem.*, 2017, **28**, 39–44.

9 (*a*) L. Yang, X. Cui, Q. Yang, S. Qian, H. Wu, Z. Bao, Z. Zhang, Q. Ren, W. Zhou, B. Chen and H. Xing, *Adv. Mater.*, 2018, **30**, 1705374; (*b*) J.-R. Wu, A. U. Mu, B. Li, C.-Y. Wang, L. Fang and Y.-W. Yang, *Angew. Chem., Int. Ed.*, 2018, **57**, 9853–9858; (*c*) Z.-T. Lin, Q.-Y. Liu, L. Yang, C.-T. He, L. Li and Y.-L. Wang, *Inorg. Chem.*, 2020, **59**, 4030–4036.

10 (*a*) T.-L. Hu, H. Wang, B. Li, R. Krishna, H. Wu, W. Zhou, Y. Zhao, Y. Han, X. Wang, W. Zhu, Z. Yao, S. Xiang and B. Chen, *Nat. Commun.*, 2015, **6**, 7328; (*b*) B. Li, X. Cui, D. O'Nolan, H.-M. Wen, M. Jiang, R. Krishna, H. Wu, R.-B. Lin, Y.-S. Chen, D. Yuan, H. Xing, W. Zhou, Q. Ren, G. Qian, M. J. Zaworotko and B. Chen, *Adv. Mater.*, 2017, **29**, 1704210; (*c*) J. Pei, K. Shao, J.-X. Wang, H.-M. Wen, Y. Yang, Y. Cui, R. Krishna, B. Li and G. Qian, *Adv. Mater.*, 2020, **32**, 1908275.

11 X. Cui, K. Chen, H. Xing, Q. Yang, R. Krishna, Z. Bao, H. Wu, W. Zhou, X. Dong, Y. Han, B. Li, Q. Ren, M. J. Zaworotko and B. Chen, *Science*, 2016, **353**, 141–144.

12 R. Matsuda, R. Kitaura, S. Kitagawa, Y. Kubota, R. V. Belosludov, T. C. Kobayashi, H. Sakamoto, T. Chiba, M. Takata, Y. Kawazoe and Y. Mita, *Nature*, 2005, **436**, 238–241.

13 S. Yang, A. J. Ramirez-Cuesta, R. Newby, V. Garcia-Sakai, P. Manuel, S. K. Callear, S. I. Campbell, C. C. Tang and M. Schröder, *Nat. Chem.*, 2015, **7**, 121–129.

14 Y.-L. Peng, T. Pham, P. Li, T. Wang, Y. Chen, K.-J. Chen, K. A. Forrest, B. Space, P. Cheng, M. J. Zaworotko and Z. Zhang, *Angew. Chem., Int. Ed.*, 2018, **57**, 10971–10975.

15 (*a*) P.-Q. Liao, W.-X. Zhang, J.-P. Zhang and X.-M. Chen, *Nat. Commun.*, 2015, **6**, 8697; (*b*) L. Li, R.-B. Lin, R. Krishna, H. Li, S. Xiang, H. Wu, J. Li, W. Zhou and B. Chen, *Science*, 2018, **362**, 443; (*c*) H. Zeng, X.-J. Xie, M. Xie, Y.-L. Huang, D. Luo, T. Wang, Y. Zhao, W. Lu and D. Li, *J. Am. Chem. Soc.*, 2019, **141**, 20390–20396; (*d*) K.-J. Chen, D. G. Madden, S. Mukherjee, T. Pham, K. A. Forrest, A. Kumar, B. Space, J. Kong, Q.-Y. Zhang and M. J. Zaworotko, *Science*, 2019, **366**, 241–246.

16 (*a*) E. D. Bloch, W. L. Queen, R. Krishna, J. M. Zadrozny, C. M. Brown and J. R. Long, *Science*, 2012, **335**, 1606–1610; (*b*) B. Li, H.-M. Wen, W. Zhou and B. Chen, *J. Phys. Chem. Lett.*, 2014, **5**, 3468–3479; (*c*) R.-B. Lin, L. Li, H.-L. Zhou, H. Wu, C. He, S. Li, R. Krishna, J. Li, W. Zhou and B. Chen, *Nat. Mater.*, 2018, **17**, 1128–1133.

17 Y.-S. Bae, O. K. Farha, A. M. Spokoyny, C. A. Mirkin, J. T. Hupp and R. Q. Snurr, *Chem. Commun.*, 2008, **35**, 4135–4137.

18 K.-J. Chen, D. G. Madden, T. Pham, K. A. Forrest, A. Kumar, Q.-Y. Yang, W. Xue, B. Space, J. J. Perry IV, J.-P. Zhang, X.-M. Chen and M. J. Zaworotko, *Angew. Chem., Int. Ed.*, 2016, **55**, 10268–10272.

19 J.-B. Lin, W. Xue, J.-P. Zhang and X.-M. Chen, *Chem. Commun.*, 2011, **47**, 926–928.

20 O. Shekhah, Y. Belmabkhout, Z. Chen, V. Guillerm, A. Cairns, K. Adil and M. Eddaoudi, *Nat. Commun.*, 2014, **5**(1), 1–7.

21 Y.-S. Bae, O. K. Farha, J. T. Hupp and R. Q. Snurr, *J. Mater. Chem.*, 2009, **19**, 2131–2134.

22 W.-Y. Gao, Y. Chen, Y. Niu, K. Williams, L. Cash, P. J. Perez, L. Wojtas, J. Cai, Y.-S. Chen and S. Ma, *Angew. Chem., Int. Ed.*, 2014, **53**, 2615–2619.

23 S.-T. Zheng, J. T. Bu, Y. Li, T. Wu, F. Zuo, P. Feng and X. Bu, *J. Am. Chem. Soc.*, 2010, **132**, 17062–17064.

24 (*a*) R.-B. Lin, L. Li, H. Wu, H. Arman, B. Li, R.-G. Lin, W. Zhou and B. Chen, *J. Am. Chem. Soc.*, 2017, **139**, 8022–8028; (*b*) J. Gao, X. Qian, R.-B. Lin, R. Krishna, H. Wu, W. Zhou and B. Chen, *Angew. Chem., Int. Ed.*, 2020, **59**, 4396–4400.

25 B. Li and B. Chen, *Chem*, 2016, **1**, 669–671.

26 T. Wang, Y.-L. Peng, E. Lin, Z. Niu, P. Li, S. Ma, P. Zhao, Y. Chen, P. Cheng and Z. Zhang, *Inorg. Chem.*, 2020, **59**, 4868–4873.

27 A. L. Myers and J. Prausnitz, Thermodynamics of mixed-gas adsorption, *AIChE J.*, 1965, **11**, 121–127.

28 G. Kresse and J. Hafner, *Phys. Rev. B: Condens. Matter Mater. Phys.*, 1993, **47**, 558–561.

29 G. Kresse and J. Furthmüller, *Phys. Rev. B: Condens. Matter Mater. Phys.*, 1996, **54**, 11169–11186.

Supplementary Information

A Robust Heterometallic Ultramicroporous MOF with Ultrahigh Selectivity for Propyne/Propylene Separation

Yun-Lei Peng,[#a,b] Ting Wang,[#a] Chaonan Jin,[d] Pengfei Li,[a] Shanelle Suepaul,[e] Gary Beemer,[f] Yao Chen,[d] Rajamani Krishna,[g] Peng Cheng,[a,c] Tony Pham,[e,f] Brian Space,[e] Michael J. Zaworotko,[b] Zhenjie Zhang*[a,c,d]

Experimental Procedures

Materials and Methods

General Methods

Pyrazine (99%, innochem), $Cu(NO_3)_2{\cdot}3H_2O$ (Analytical reagent, Gerhardite), $(NH_4)_2{\cdot}SiF_6$ (Analytical reagent, Greagent), 4,4'-bipyridylacetylene (95+%, HUAWEIRUIKE), 4,4' -azopyridine (95+%, HUAWEIRUIKE), $CuSiF_6$ (Analytical reagent, Greagent), $Ni(BF_4)_2{\cdot}6H_2O$ (Energy chemical), 2,3-dichloropyrazine (98%, Bide Pharmatech Ltd), Sodium hydroxide (NaOH, 97%, Aladdin), Sodium hydrosulfide (NaHS, LiDeShi), Copper(II) perchlorate hexahydrate ($Cu(ClO_4)_2.6H_2O$, 98%, Strem Chemical, Inc.), Nickel(II) iodide (NiI_2, >99.5%, aladdin), iodide (I_2, AR, TIANJINGFENGCHUAN), acetonitrile, ether, and acetone were purchased and used without further purification. He, N_2, C_3H_4 and C_3H_6, were purchased from AIR LIQUIDE. The powder X-ray diffraction data were obtained on ULTIMA IV. Fourier transform infrared spectra (FT-IR) were recorded on Nicolet IS10.

Synthesis of metal-ligand $Na[Cu(pdt)_2]{\cdot}2H_2O$

The ligand was synthesized based on the previous method.[1]

Synthesis of SIFSIX-3-Ni $(Ni(pyrazine)_2SiF_6)_n$

SIFSIX-3-Ni were prepared based on previously reported procedures.[2a]

Synthesis of SIFSIX-2-Cu-i $(Cu(4,4'\text{-bipyridylacetylene})_2SiF_6)_n$

SIFSIX-2-Cu-i were prepared based on previously reported procedures.[2b]

Synthesis of SIFSIX-14-Cu-i (UTSA-200) $(Cu(4,4'\text{ -azopyridine})_2SiF_6)_n$

SIFSIX-14-Cu-i were prepared based on previously reported procedures. [2a]

Powder X-ray diffraction (PXRD) analysis:

Powder x-ray diffraction test was conducted using microcrystalline samples on a Rigaku Ultima IV diffractometer (40 kV, 40 mA, CuKα1, 2 λ = 1.5418 Å). The measured parameter included a scan speed of 2(°)/min, a step size of 0.02(°).

Field emission scanning electron microscope (FE-SEM) analysis:

The morphologies of **NKMOF-11** were characterized via field-emission scanning electron microscopy (SEM, JEOL JSM7500F, 5 kV and Phenom XL, 15 kV). The SEM–energy dispersive spectroscopy (EDS) of the samples are collected with Phenom XL at an acceleration voltage of 15 kV.

Inductively Coupled Plasma Optical Emission Spectro analysis

The metal element ratio in **NKMOF-11** was characterized by ICP-OES(SPECTRO-BLUE).

Fitting of single-component adsorption isotherm and Isosteric Heat of Adsorption

The experimental isosteric heat of adsorption (Q_{st}) values for various gases in **NKMOF-11** were determined by first fitting the adsorption isotherms at 273 K, 298 K, 308 K and 318 K for the respective adsorbates to the dual-site Langmuir-Freundlich (**DSLF**) equation,[3] subsequently applying the Clausius-Clapeyron method.[4] The **DSLF** equation is given by:

$$n = \frac{n_{m1} b_1 P^{\left(\frac{1}{t_1}\right)}}{1 + b_1 P^{\left(\frac{1}{t_1}\right)}} + \frac{n_{m2} b_2 P^{\left(\frac{1}{t_2}\right)}}{1 + b_2 P^{\left(\frac{1}{t_2}\right)}} \quad \text{(DSLF)} \qquad (1)$$

where n is the uptake (in mmol g^{-1}), P is the pressure (in kPa), n_{m1} and n_{m2} are the saturation uptakes (in mmol g^{-1}) for sites 1 and 2, b_1 and b_2 are the affinity coefficients (in kPa^{-1}) for sites 1 and 2, and t_1 and t_2 represent the deviations from the ideal homogeneous

surface (unit less) for sites 1 and 2. The parameters that were obtained from the fitting of the C_3H_4 and C_3H_6 adsorption isotherms are found in**Tables S1** and **S2,** respectively.
The fitted parameters were used to calculate the Q_{st} values for a range of uptakes through the Clausius–Clapeyron equation, which is the following:

$$Q_{st} = -R\frac{\partial \ln P}{\partial\left(1/T\right)} \quad (2)$$

Where *T* is the temperature (in K) and *R* is the ideal gas constant. The partial derivative term actually represents the slope of the plot of ln *P vs.* 1/*T* for a number of isotherms at different temperatures at various loadings. Therefore, the above Q_{st} equation can be simplified to:

$$Q_{st} = -mR \quad (3)$$

where *m* is the slope, which can be calculated by the following for *x* (2 or 3) different temperatures and their corresponding pressures:

$$m = \frac{\sum\frac{1}{T_i}\ln P_i - \frac{1}{x}\left(\sum\frac{1}{T_i}\right)\left(\sum \ln P_i\right)}{\sum\left(\frac{1}{T_i}\right)^2 - \frac{1}{x}\left(\sum\frac{1}{T_i}\right)^2} \quad (4)$$

The P_i values were back-calculated for a range of uptakes using the DSLF equation *via* an iterative technique (e.g., the Newton–Raphson method).[5]
The experimental C_3H_6 and C_3H_4 Q_{st} for **NKMOF-11** were also determined through a simultaneous fitting to the DSLF equation,[5] Notably, b_1 and b_2 are expressed as a function of temperature via the following:

$$b_1 = b_{01}e^{\left(\frac{E1}{RT}\right)} \quad (5)$$

$$b_2 = b_{02}e^{\left(\frac{E2}{RT}\right)} \quad (6)$$

where R is the ideal gas constant, b_{01} and E_1 are the pre-exponential factor (in kPa^{-1}) and the activation energy (in kJ mol^{-1}) for site 1, and b_{02} and E_2 are analogous parameters for site 2. The parameters obtained for the simultaneous fitting of the experimental C_3H_6 and C_3H_4 adsorption isotherms at 298 and 308 K in **NKMOF-11** are provided in **Tables S3 and S4**. These parameters were used to calculate the Q_{st} values for a range of uptakes using the following form of the Clausius-Clapeyron equation:

$$Q_{st} = \frac{-RT_1T_2}{T_2 - T_1}\ln\left(\frac{P_1}{P_2}\right) \quad (7)$$

Results and Discussion

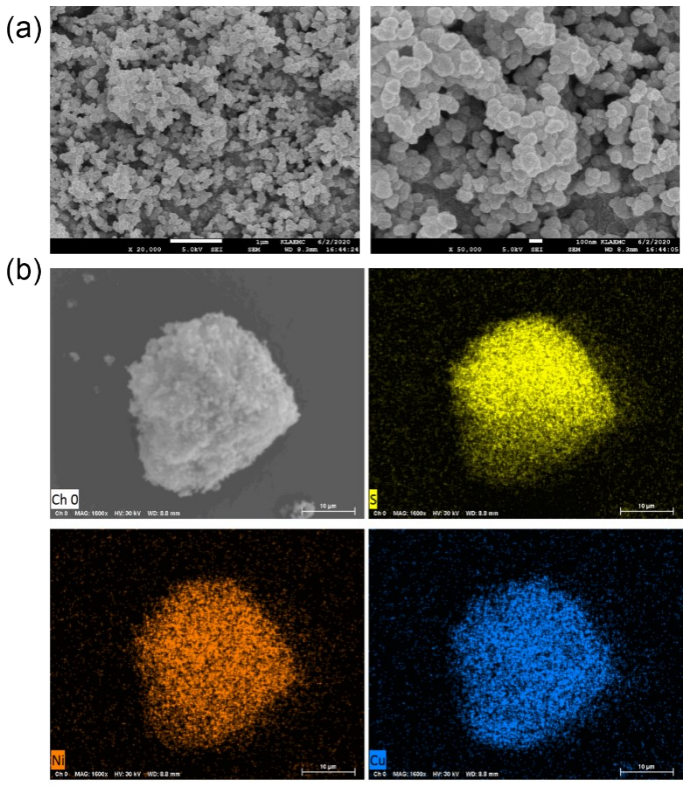

Fig. S1 (a) The field emission scanning electron microscope (FE-SEM) images of **NKMOF-11**; (b) The elemental mapping of **NKMOF-11**.

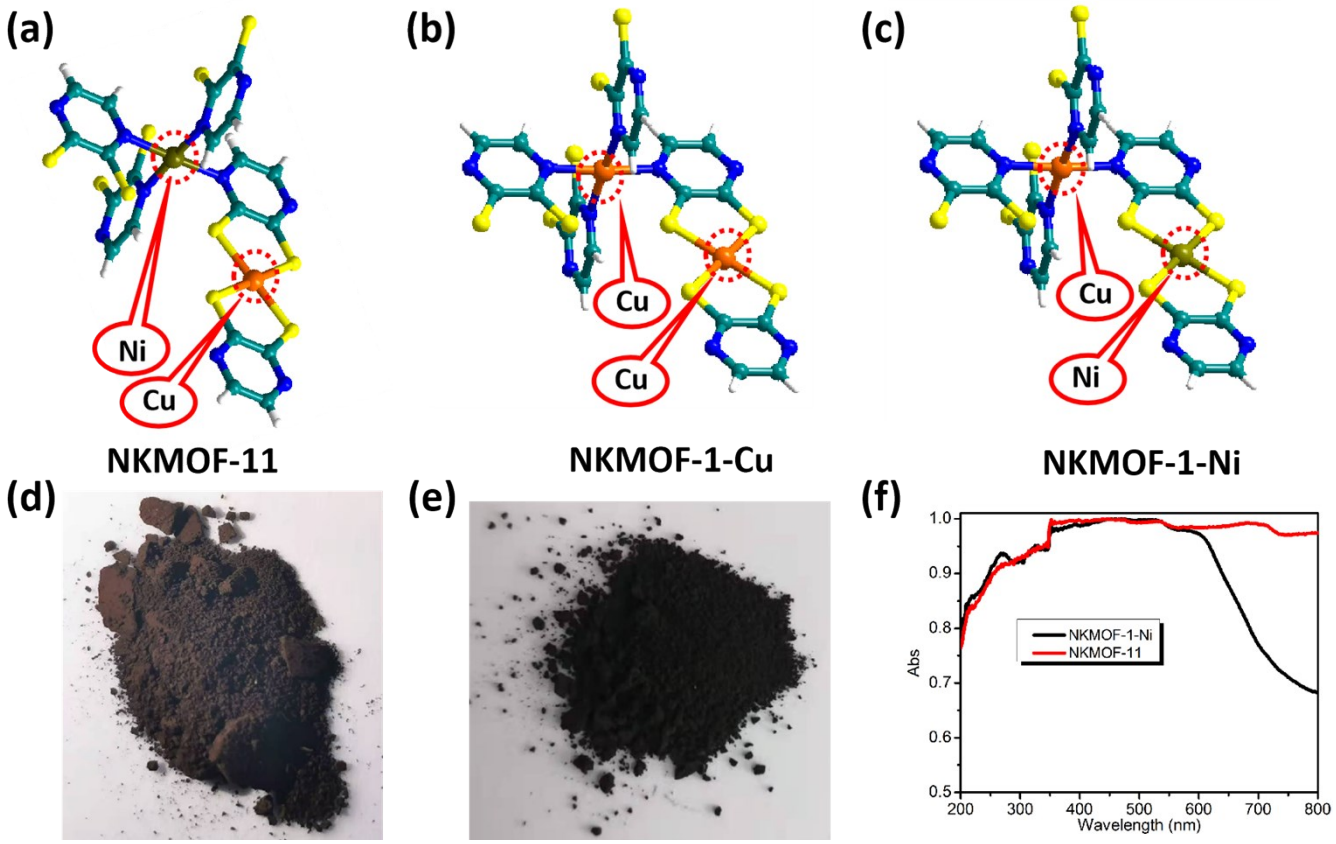

Fig. S2 (a) The coordination environment of metals in **NKMOF-11**.; (b) The coordination environment of metals in **NKMOF-1-Cu**; (c) The coordination environment of metals in **NKMOF-1-Ni; (d) The appearance of NKMOF-1-Ni; (e) The appearance of NKMOF-11; (F) The solid UV-Vis spectra of NMOF-11 and NKMOF-1-Ni.**

(a)

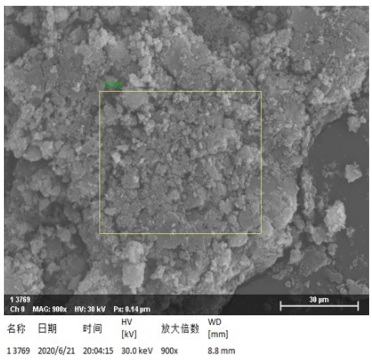

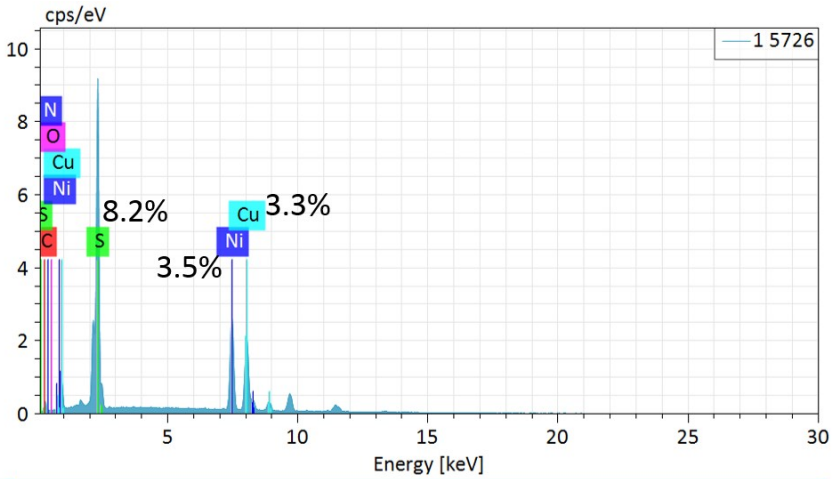

(b)

Instrument	ICP-OES（SPECTRO-BLUE）	
Testing Results (wt%)		
NKMOF-11	Cu	Ni
1	14.82	15.31
2	15.25	14.92
3	14.96	15.34
Average	15.01	15.19

Fig. S3 (a) Energy Dispersive X-ray Spectrometric Microanalysis (EDX) of **NKMOF-11**; (b) Inductively Coupled Plasma Optical Emission Spectro of **NKMOF-11**.

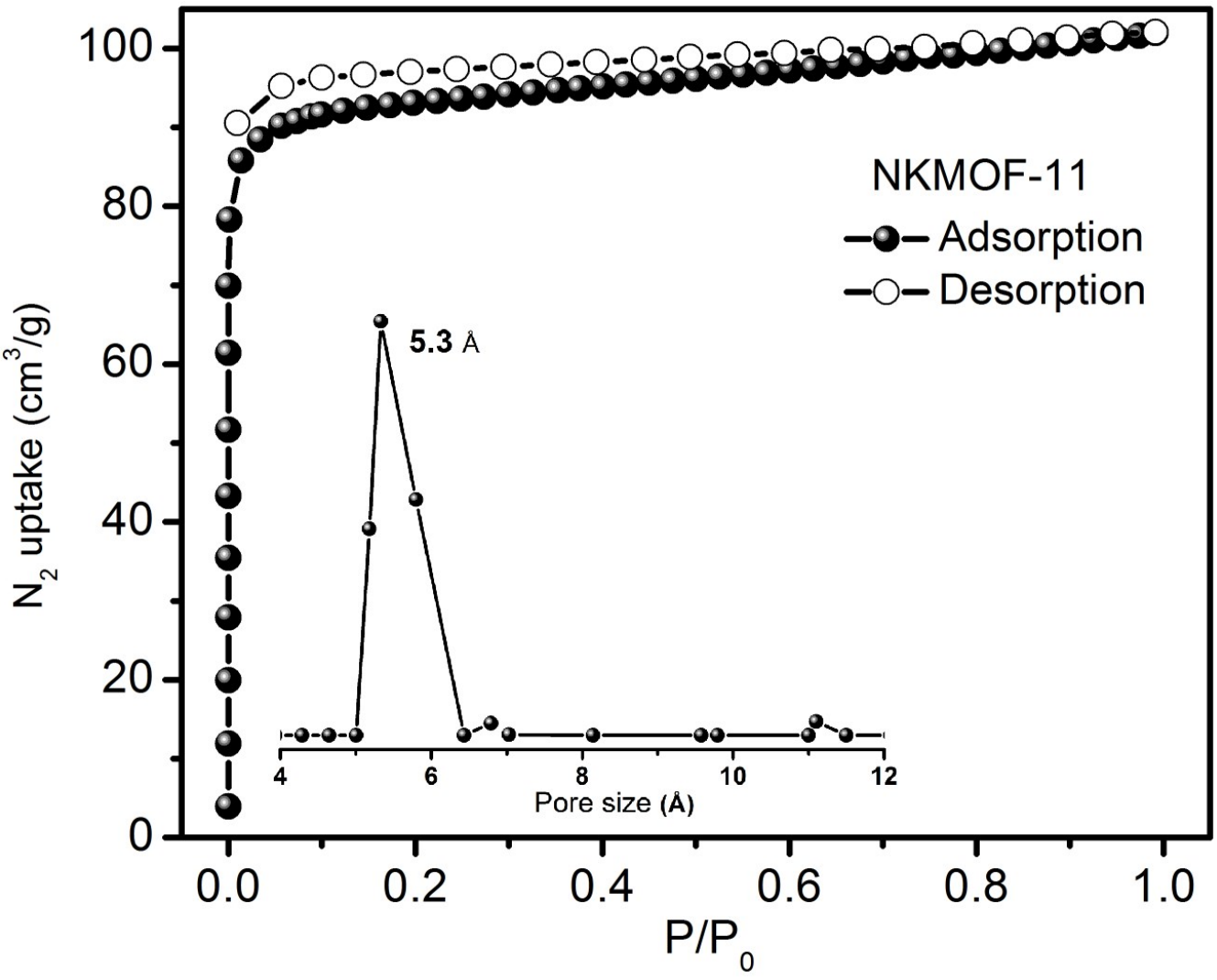

Fig. S4 N_2 adsorption isotherm and pore size distribution of **NKMOF-11** at 77 K.

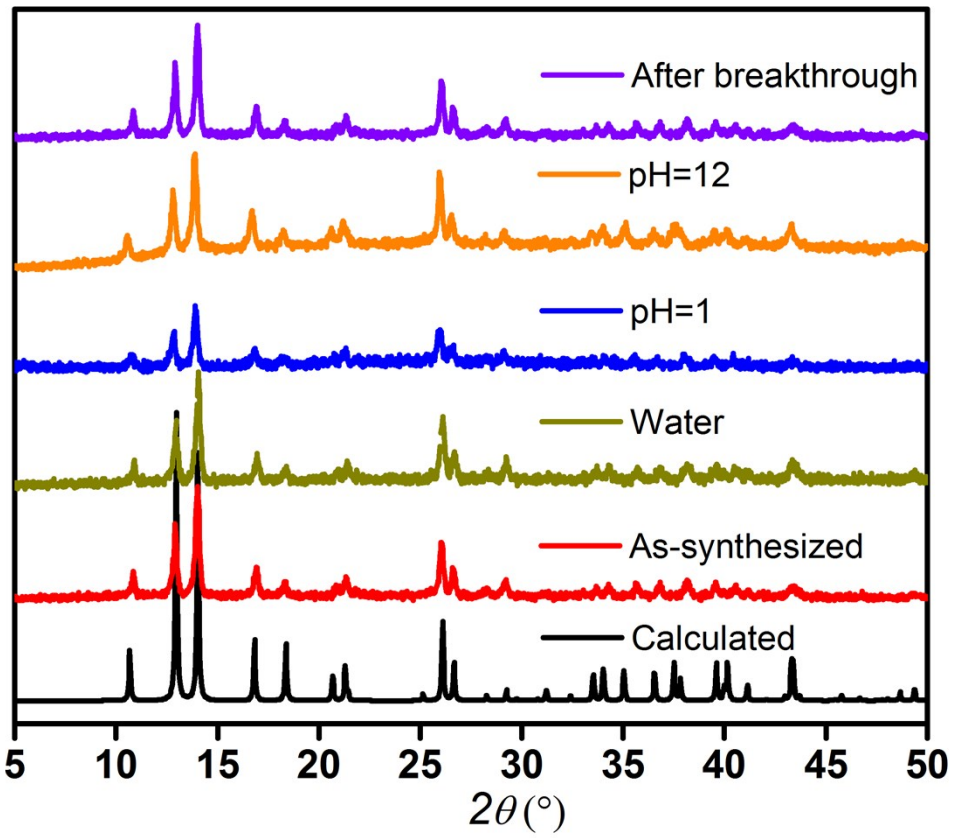

Fig. S5 PXRD patterns showing the exceptional structural stability of **NKMOF-11**. Pristine **NKMOF-11** (red); **NKMOF-11** soaked in pure water for 2 year (dark yellow); **NKMOF-11** soaked in pH=1 aqueous solution (blue); **NKMOF-11** soaked in pH=12 aqueous solution(orange); after fifth breakthrough (violet).

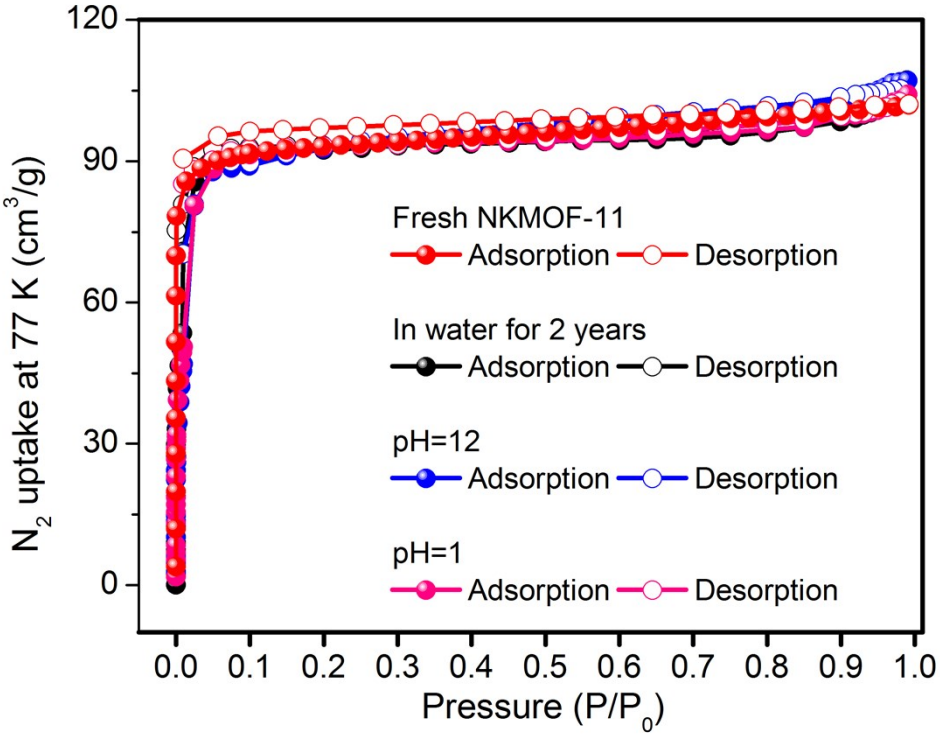

Fig. S6 The schematic of measured BET (N_2) of **NKMOF-11**. Pristine **NKMOF-11** (black); **NKMOF-11** soaked in pure water for 2 year (red); **NKMOF-11** soaked in pH=12 aqueous solution (blue); **NKMOF-11** soaked in pH=1 aqueous solution (pink).

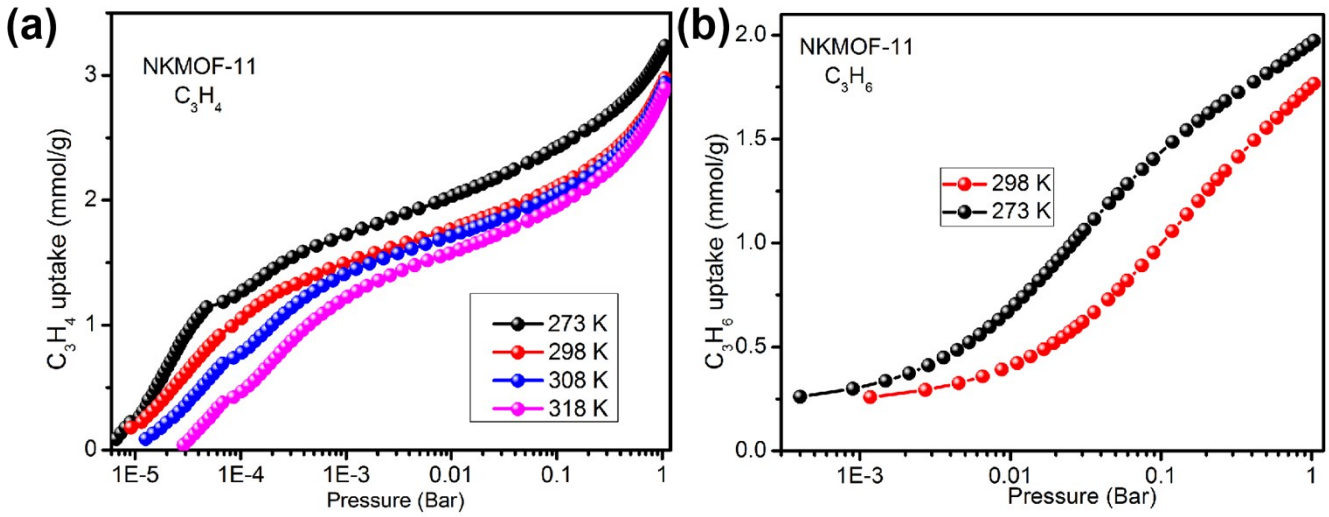

Fig. S7 The schematic of C_3H_4 and C_3H_6 single component gas adsorption isotherm for **NKMOF-11**. (a) C_3H_4 for **NKMOF-11**. (b) C_3H_6 for **NKMOF-11**.

Table S1. The fitted parameters for the DSLF equation for the C_3H_4 adsorption isotherms for **NKMOF-11** at 298, 308, and 318 K. The R^2 values are also provided.

Parameter	**298 K**	**308 K**	**318 K**
n_{m1} (mmol g^{-1})	2341.9304	3368.4332	809.9221
b_1 (kPa^{-1})	1.2345E-04	5.3343E-05	2.4600 E-04
t_1	2.9055	2.3330	2.3626
n_{m2} (mmol g^{-1})	1.4602	1.5540	1.4067
b_2 (kPa^{-1})	240.3585	61.2466	58.1809
t_2	0.9708	1.0898	0.9335
R^2	0.9983	0.9985	0.9988

Table S2. The fitted parameters for the DSLF equation for the C_3H_6 adsorption isotherms for **NKMOF-11** at 273, and 298 K. The R^2 values are also provided.

Parameter	**273 K**	**298 K**
n_{m1} (mmol g^{-1})	3.4448	1.6770
b_1 (kPa^{-1})	1.6400E-02	2.4200E-02
t_1	2.0773	1.8672
n_{m2} (mmol g^{-1})	1.3275	1.3183

b_2 (kPa^{-1})	0.4384	0.12364
t_2	1.0610	1.1266
R^2	0.9999	0.9999

Table S3. DSLF parameter fits for C_3H_6 in **NKMOF-11** as obtained through simultaneous fitting of the adsorption isotherms at 273 and 298 K.

	Site 1				Site 2				
	n_{m1}	b_{01}	E_1	t_1	n_{m2}	b_{02}	E_2	t_2	R^2
NKMOF-11	0.4080	3.62E-07	17.74683	0.6711	1.6247	3.70E-07	31.5227	1.16112	0.9999

Table S4. DSLF parameter fits for C_3H_4 in **NKMOF-11** as obtained through simultaneous fitting of the adsorption isotherms at 298 and 308 K.

	Site 1				Site 2				
	n_{m1}	b_{01}	E_1	t_1	n_{m2}	b_{02}	E_2	t_2	R^2
NKMOF-11	1.5367	3.29E-08	54.9751	1.0609	25.3496	1.65E-03	4.0528	2.4294	0.9982

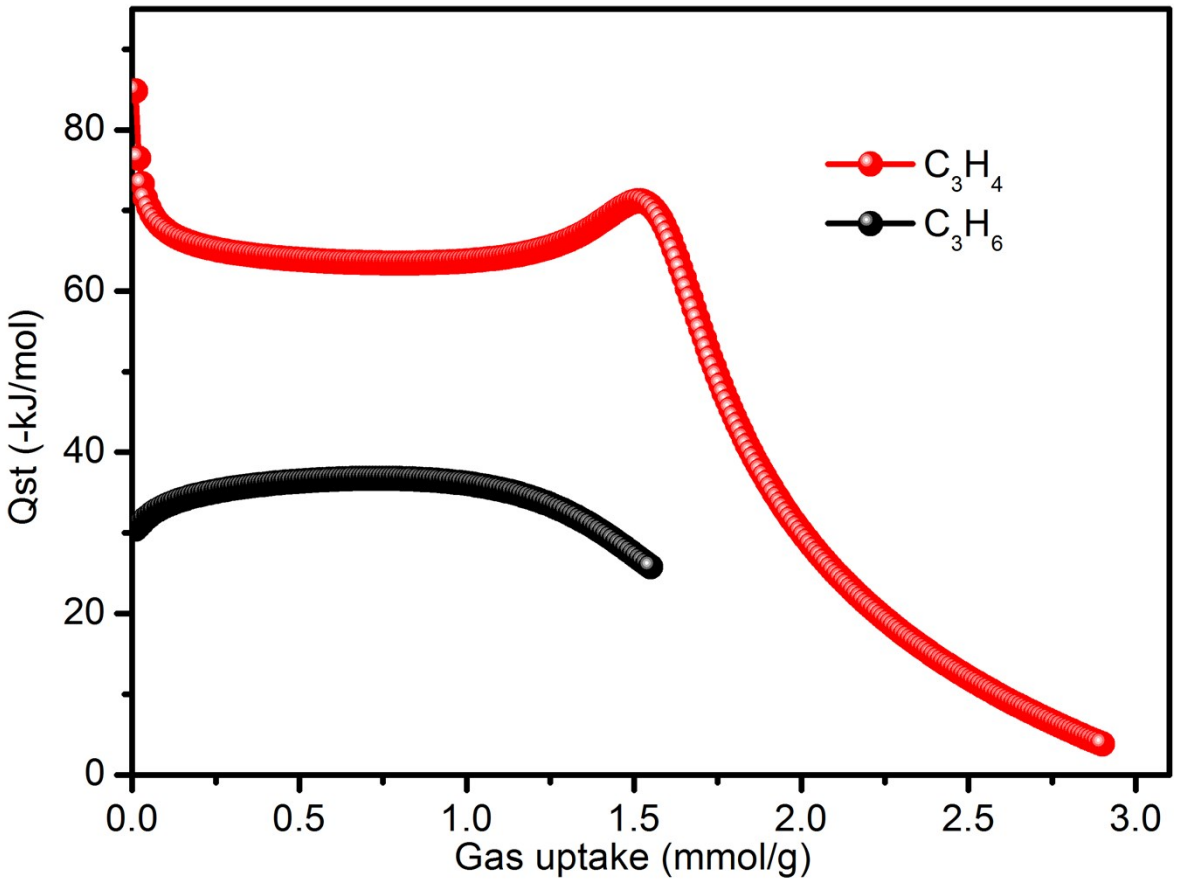

Fig. S8 Q_{st} curves of C_3H_4 and C_3H_6 for and **NKMOF-11** as obtained using Clausius-Clapeyron equation.

Table S5. Breakthrough calculations for separation of C_3H_4/C_3H_6 (1/99 and 1/999 (v/v)) mixture at 298 K.

Sorbent	Breakthrough productivity of C_3H_6 (mol/L)	
	C_3H_4/C_3H_6 (1/99, v/v)	C_3H_4/C_3H_6 (1/999, v/v)
NKMOF-11	271.7	1404.7
SIFSIX-3-Ni	185.6	285.1
SIFSIX-2-Cu-i	51.0	57.3
ELM-12[28]	94.6	110.2
ZU-62[29]	123.2	184.2

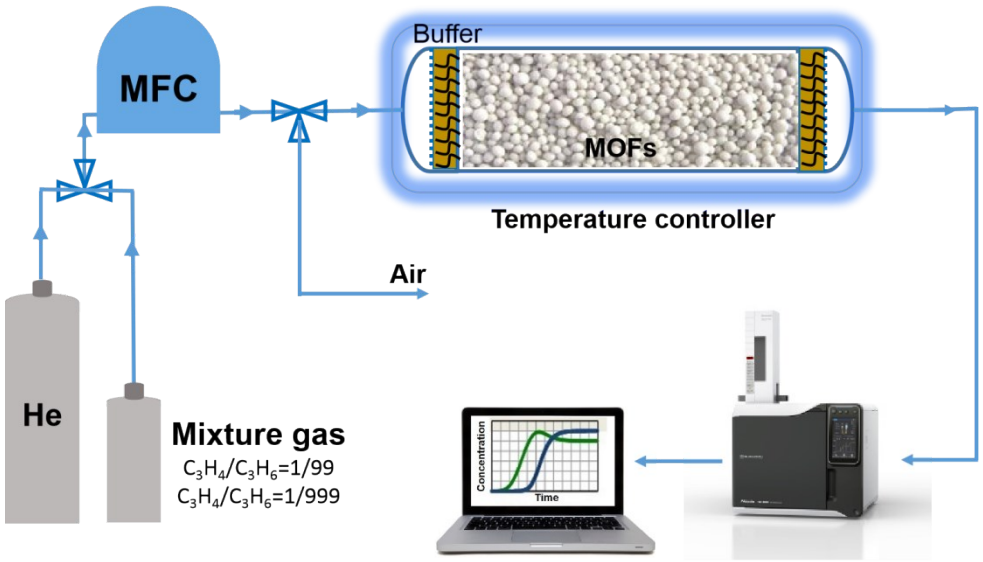

Scheme S1. Breakthrough separation apparatus.

Table S6. Comparisons of the breakthrough columns parameters studied in this work.

Sorbent	Sample weight (g)	Crystal density (g/cm^3)	Packing density (g/cm^3)	Column voidage	Column free space (cm^3)
NKMOF-11	0.102	1.713	0.850	0.504	0.060
SIFSIX-3-Ni	0.105	1.770	0.875	0.506	0.061
SIFSIX-2-Cu-i	0.103	1.423	0.858	0.397	0.048

[a] Packing density = Sample weight / Column volume (The valid column volume in this work is 0.12 cm^3).

[b] Column voidage = 1- Sample weight / Crystal density / Column volume.

[c] Column free space = Column volume × Column voidage.

Table S7. Comparisons of pure C_3H_6 (C_3H_4 < 0.1 ppm) productivities in a single breakthrough operation using C_3H_4/C_3H_6 (1/99 v/v) and (1/999 v/v) mixtures as input.

Sorbent	Crystal density (g/cm^3)	Gravimetric/Volumetric C_3H_6 Productivity (mmol/g and mmol/cm^3) of different gases mixtures	
		C_3H_4/C_3H_6 (1/99 v/v) (C_3H_4 < 1 ppm)	C_3H_4/C_3H_6 (1/999 v/v) (C_3H_4 < 1 ppm)
NKMOF-11	1.713	74.4/127.5	165.1/282.7
SIFSIX-3-Ni	1.770	--	69.5/123.0
SIFSIX-2-Cu-i	1.423	29.0/41.2	--
UTSA-200[2c]	1.417	62.05 / 87.92	142.86 / 202.43

Modeling Studies

A. Parametrization

The single X-ray crystallographic structure that was collected herein for **NKMOF-11** was used for the parametrizations and simulations in this work.

For the purpose of classical molecular simulations of propyne, and propylene adsorption in **NKMOF-11**, all atoms of the MOF were given Lennard-Jones 12–6 parameters (ε and σ),[6] point partial charges, and scalar point polarizabilities to model repulsion/dispersion, stationary electrostatic, and many-body polarization interactions, respectively. The Lennard-Jones parameters for all C and H atoms were taken from the Optimized Potentials For Liquid Simulations – All Atom (OPLS-AA) force field,[7] while such parameters for the N, S, Ni, and Cu atoms were taken from the Universal Force Field (UFF).[8]

The crystal structure of **NKMOF-11** contains 7 atoms in chemically distinct environments (**Fig. S9**). The partial charges for each unique atom were determined through electronic structure calculations on different gas phase fragments that were selected from the crystal structure of the MOF. For these calculations, all C, H, N, and S atoms were treated with the 6-31G* basis set,[9] while the LANL2DZ ECP basis set[10] was used for the Cu^{2+} and Ni^{2+} ions. The NWChem *ab initio* simulation package[11]was used to calculate the electrostatic potential surface for each fragment and the partial charges were subsequently fitted onto the atomic positions of the fragments using the CHELPG method.[12] For each chemically distinct atom, the partial charges were averaged between the fragments. The partial charges were then adjusted so that the total charge of the system was equal to zero. The resulting partial charges for each chemically distinguishable atom in **NKMOF-11** are provided in **Table S8**. The exponential damping-type polarizability values for all C, H, N, and S atoms were taken from a carefully parametrized set provided by the work of van Duijnen and Swart.[13] The polarizability parameter for Ni^{2+} and Cu^{2+} were determined in previous work[14]and used for the simulations herein.

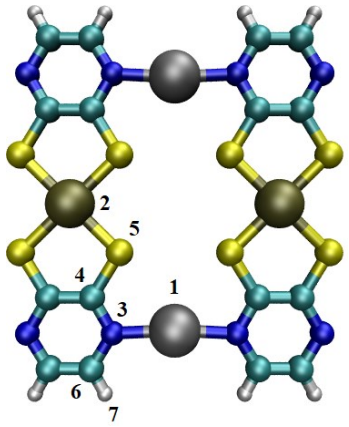

Fig. S9. The numbering of the chemically distinct atoms in **NKMOF-11** as referred to in **Table S8**. Atom colors: C = cyan, H = white, N = blue, S = yellow, Ni = silver, Cu = gold.

Table S8: The partial charges (in e^-) for the chemically distinct atoms in **NKMOF-11** that were used for the GCMC simulations in this work. Label of atoms correspond to **Figure S8**.

Atom	Label	*q* (e^-)
Ni	1	1.3031
Cu	2	0.5737
N	3	–0.5272
C	4	0.2001
S	5	–0.2983
C	6	0.0380
H	7	0.1182

B. Grand Canonical Monte Carlo

Molecular simulations of propyne and propene adsorption were performed in **NKMOF-11** using grand canonical Monte Carlo (GCMC) methods [15] within a 3 × 3 × 2 supercell of the MOF. A spherical cut-off distance of 10.2396 Å was used for the simulations; this value corresponds to half the shortest supercell dimension length. Propyne, and propylene were modeled using recently developed polarizable potentials of the respective adsorbates.[16] The total potential energy of the MOF-adsorbate system was calculated through the sum of the repulsion/dispersion, stationary electrostatic, and polarization energies. These were calculated using the Lennard-Jones 12-6 potential, partial charges with Ewald summation,[17] and a Thole-Applequist type model,[18] respectively. All MOF atoms were kept fixed throughout the simulations. All GCMC simulations were performed using the Massively Parallel Monte Carlo (MPMC) code.[19]

According to the simulations, saturation of propyne and propene in **NKMOF-11** is achieved at 2.5 and 2 molecules per unit cell, respectively. The modeled 3 × 3 × 2 supercell of the MOF containing the saturated loading amount for propyne and propene are shown in **Fig. S10** and **S11**, respectively. Consistent with previous experimental and theoretical findings for these adsorbates in the isostructural **NKMOF-1-Cu** and **NKMOF-1-Ni**, all C3 hydrocarbons adsorbed at two main binding sites in **NKMOF-11**: (1) between the pyrazine units and (2) between the CuS_4 units.

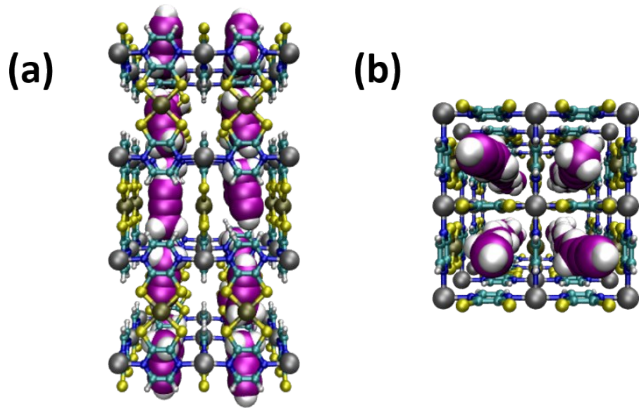

Fig. S10 (a) Perspective *a/b*-axis view and (b) *c*-axis view of the modeled 3 × 3 × 2 supercell in **NKMOF-11** at propyne saturation. Atom colors: C(MOF) = cyan, C(propyne) = magenta, H = white, N = blue, S = yellow, Ni = silver, Cu = gold.

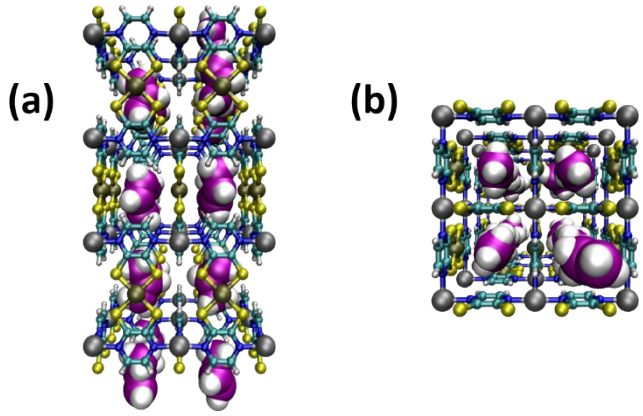

Fig. S11 (a) Perspective *a/b*-axis view and (b) *c*-axis view of the modeled 3 × 3 × 2 supercell in **NKMOF-11** at propene saturation. Atom colors: C(MOF) = cyan, C(propene) = magenta, H = white, N = blue, S = yellow, Ni = silver, Cu = gold.

C. Density Functional Theory

Periodic density functional theory (DFT) calculations were performed to evaluate the adsorption energy (ΔE) for propyne, and propylene about the two adsorption sites in **NKMOF-11**. These calculations were performed using the Vienna *ab initio* Simulation Package (VASP)[20] with the projector augmented wave (PAW) method,[21] Perdew-Burke-Ernzerhof (PBE) functional,[22] and the DFT-D2 correction method of Grimme.[23] For both sites, the position of a single molecule of each adsorbate was initially optimized within the rigid unit cell of the MOF. Afterward, another optimization was carried out in which the position of all atoms and lattice parameters of the system were allowed to vary. All optimizations were converged to within 10^{-6} eV. The optimized position of a propyne, and propylene molecule about both sites within **NKMOF-11** are displayed in **Fig. 5,** and **Fig. S12**, respectively.

The ΔE for the adsorbates localized about the two binding sites in **NKMOF-11** were calculated by the following:
$\Delta E = E(\text{MOF + Adsorbate}) - E(\text{MOF}) - E(\text{Adsorbate})$
where E(MOF + Adsorbate) is the energy of the unit cell of the MOF with the adsorbate, E(MOF) is the energy of the empty unit cell, and E(Adsorbate) is the energy of the adsorbate. The calculated ΔE values for propyne, and propene about both sites in **NKMOF-11** are listed in **Table S9**.

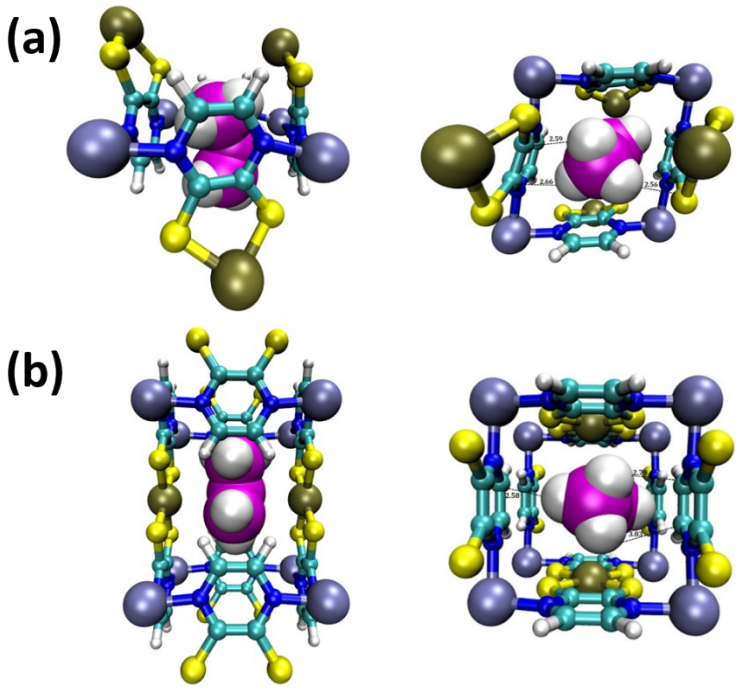

Fig. S12 Perspective views (left = *a*/*b*-axis, right = *c*-axis) of a portion of the crystal structure of **NKMOF-11** showing the optimized position of a propylene molecule about (a) the pyrazine units and (b) the CuS_4 units in the MOF as determined through periodic DFT calculations using VASP. The closest MOF-adsorbate distances are also shown. Atom colors: C(MOF) = cyan, C(propylene) = magenta, H = white, N = blue, S = yellow, Ni = silver, Cu = gold.

Table S9. Calculated adsorption energies (in kJ mol^{-1}) for a single propyne, and propylene molecule at two sites in **NKMOF-11** as determined from periodic DFT calculations using VASP. Site 1 corresponds to adsorption between the pyrazine units and site 2 is between the CuS_4 units.

Adsorbate	**Site**	**Δ*E* (kJ mol^{-1})**
Propyne	1	–70.09
	2	–54.11
Propylene	1	–43.32
	2	–55.68

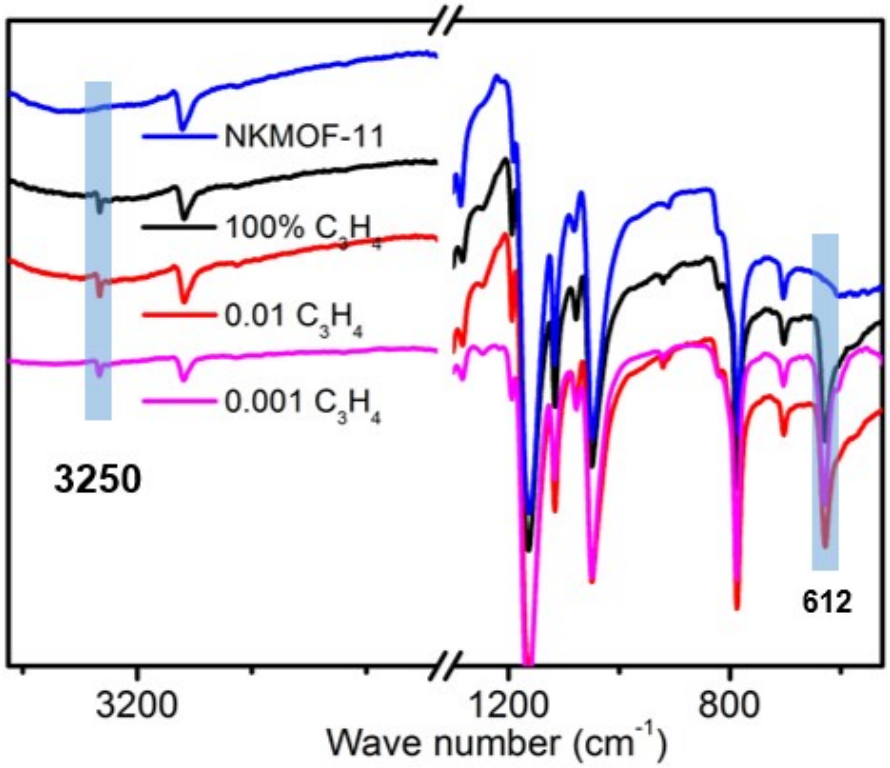

Fig. S13 The schematic of FT-IR of **NKMOF-11** absorbed C_3H_4 from gas mixture containing C_3H_4. Two characteristic peaks of C_3H_4 were highlighted in blue.

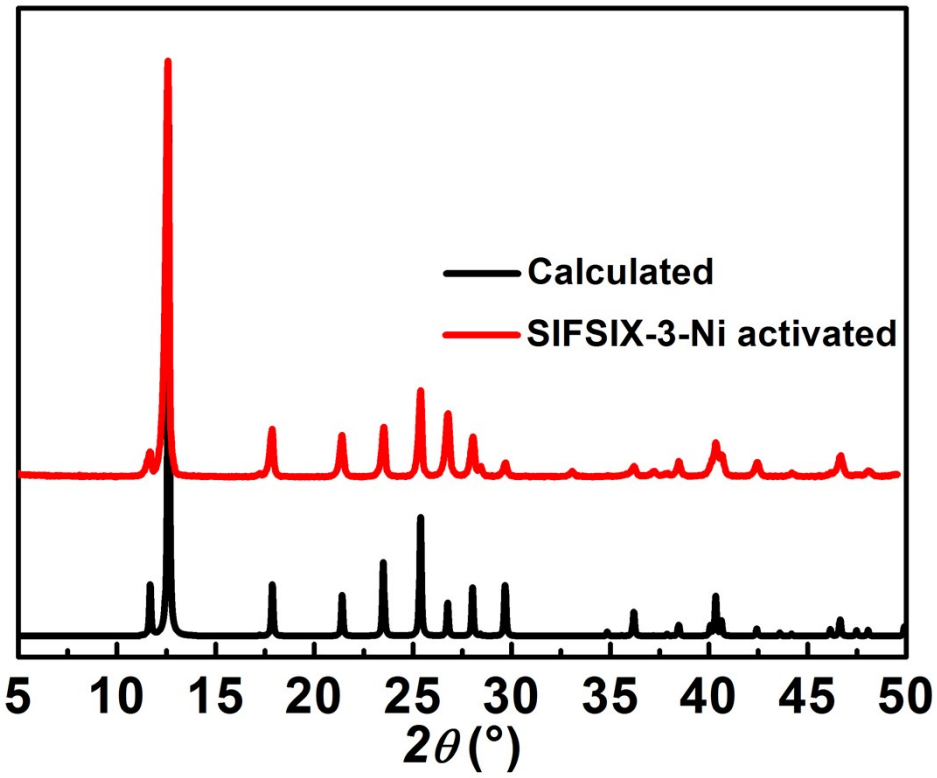

Fig. S14 PXRD patterns of the calculated and activated **SIFSIX-3-Ni**.

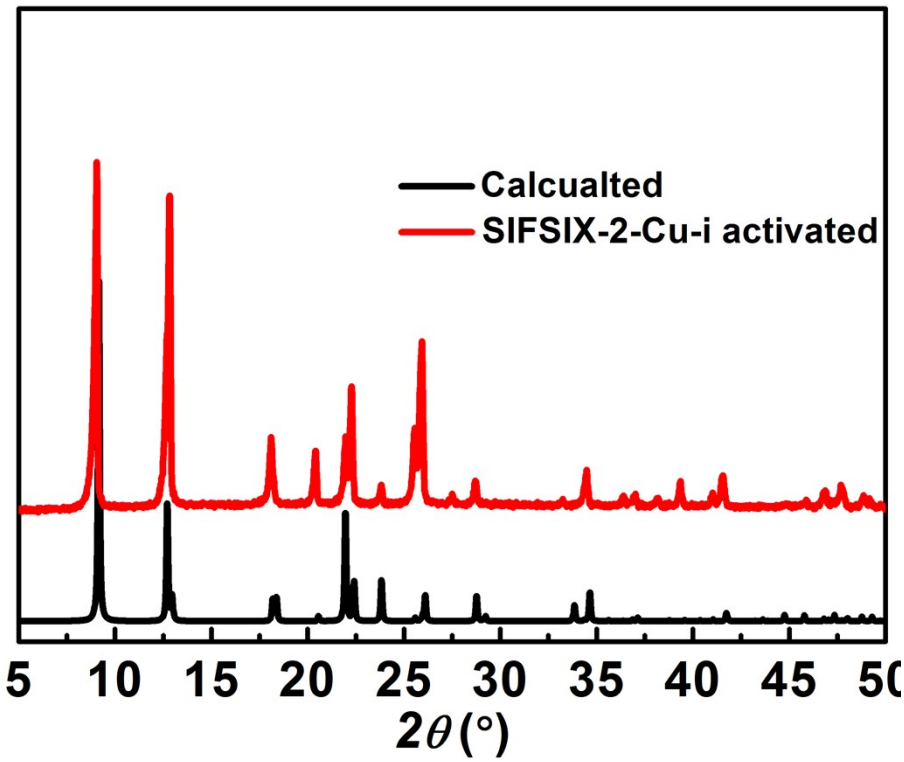

Fig. S15 PXRD patterns of the calculated, activated **SIFSIX-2-Cu-i**.

Simulated transient breakthrough of mixtures in fixed bed adsorbers

The performance of industrial fixed bed adsorbers is dictated by a combination of adsorption selectivity and uptake capacity. Transient breakthrough simulations were carried out for 1/99 $C_3H_4(1)/C_3H_6$ and 1/999 $C_3H_4(1)/C_3H_6$ mixtures operating at a total pressure of 100 kPa and 298 K, using the methodology described in earlier publications.[24-27] For the breakthrough simulations, the following parameter values were used: length of packed bed, *L* = 0.3 m; voidage of packed bed, ε = 0.4; superficial gas velocity at inlet, μ = 0.04 m/s.

The transient breakthrough simulation results are presented in terms of a *dimensionless* time, τ, defined by dividing the actual time, *t*, by the characteristic time, $L\varepsilon/u$.

For comparisons of the separation performance, we plot the ppm C_3H_4 in the gaseous product mixture leaving the adsorber as a function of the dimensionless time, τ. The breakthrough data are provided in Figure 3.

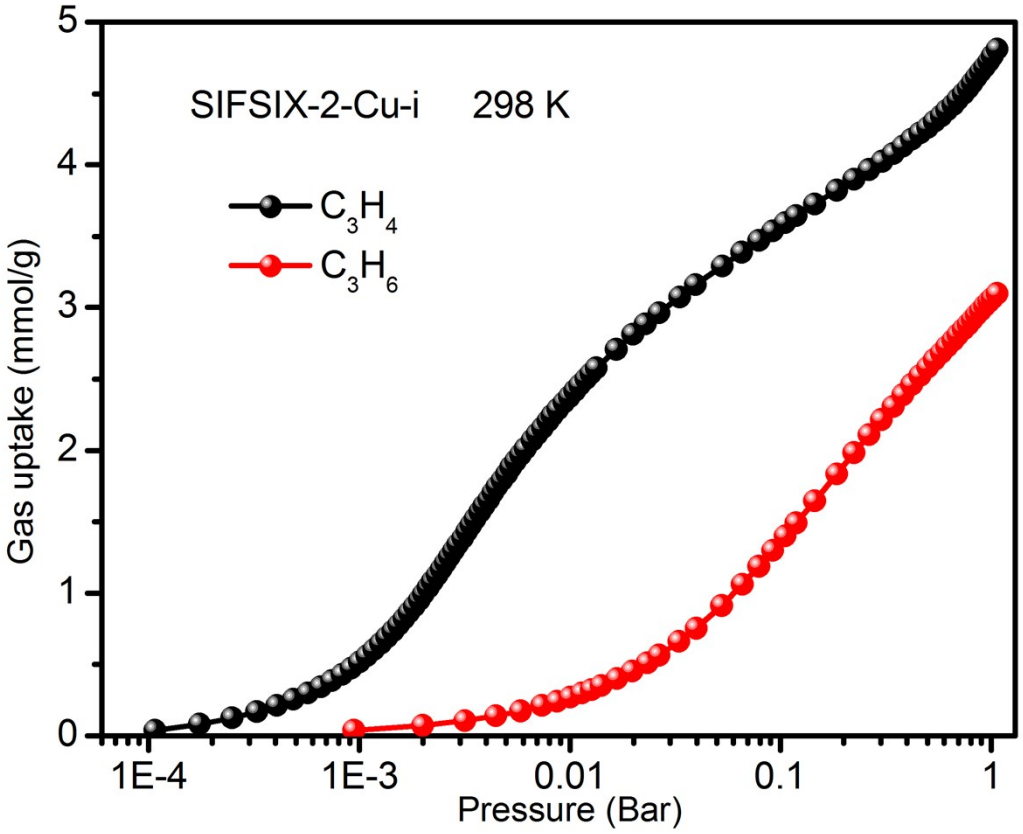

Fig. S16 The schematic of C_3H_4 and C_3H_6 gas adsorption isotherms for **SIFSIX-2-Cu-i** at 298 K.

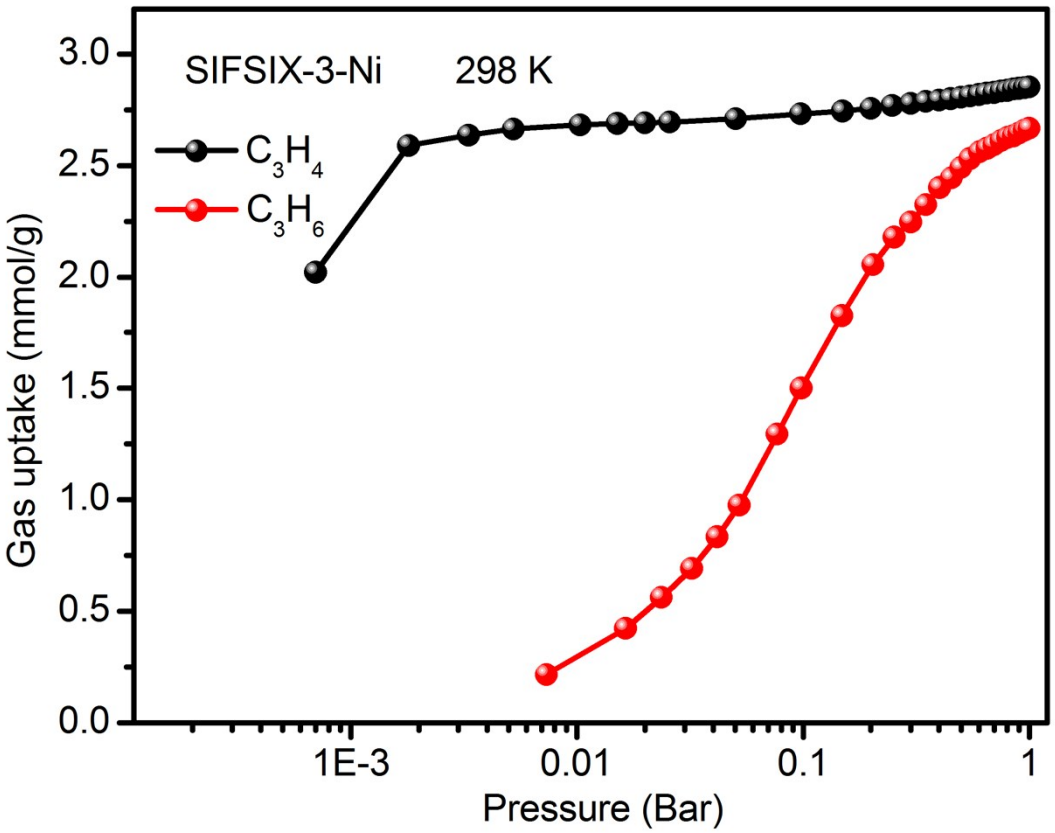

Fig. S17 The schematic of C_3H_4 and C_3H_6 gas adsorption isotherm for **SIFSIX-3-Ni** at 298 K.

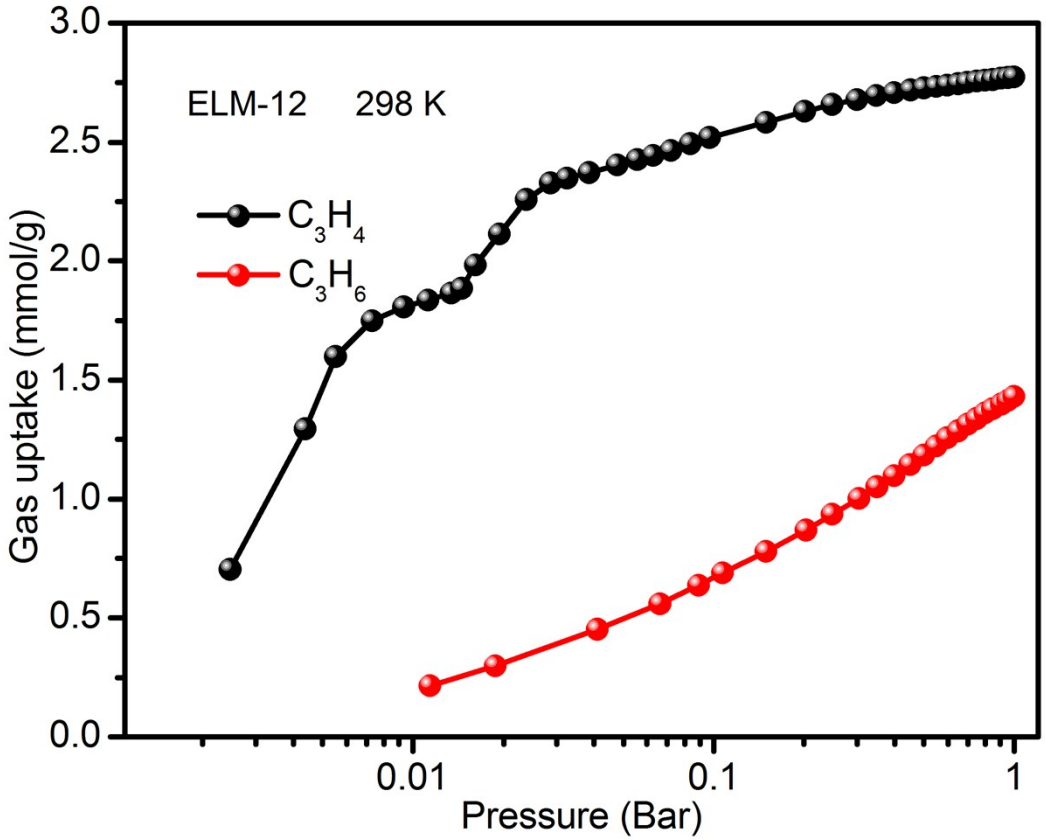

Fig. S18 The schematic of C_3H_4 and C_3H_6 gas adsorption isotherm for **ELM-12** at 298 K.

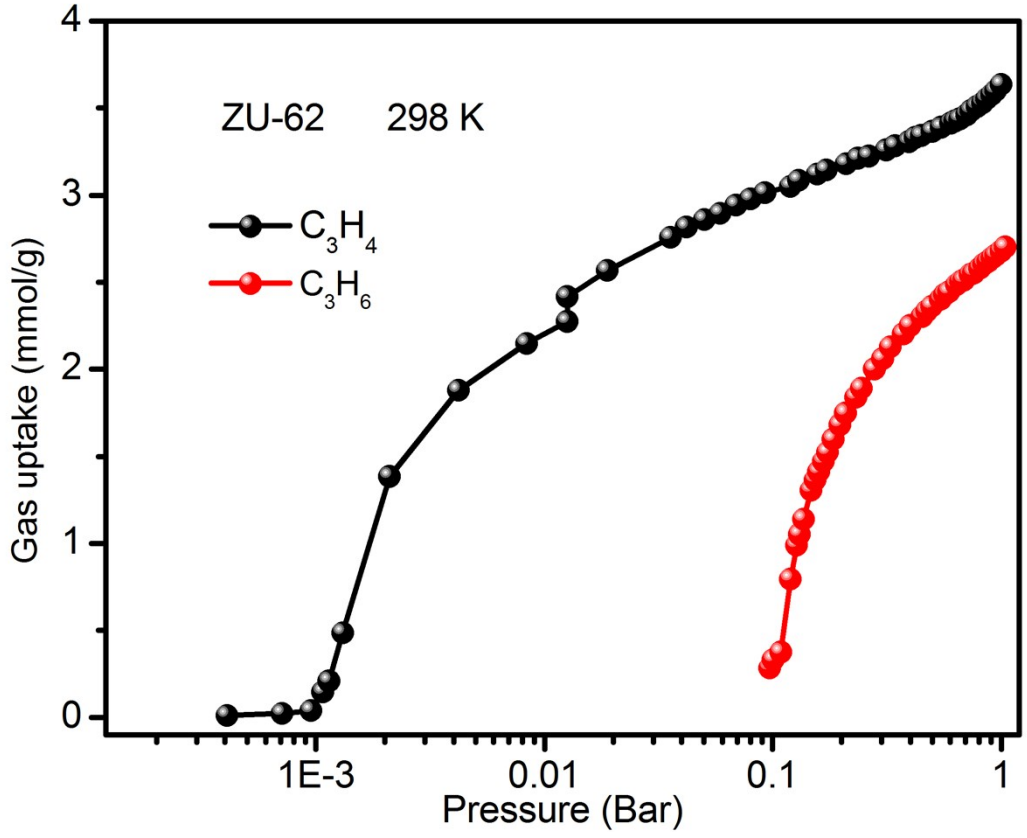

Fig. S19 The schematic of C_3H_4 and C_3H_6 gas adsorption isotherm for **ZU-62** at 298 K.

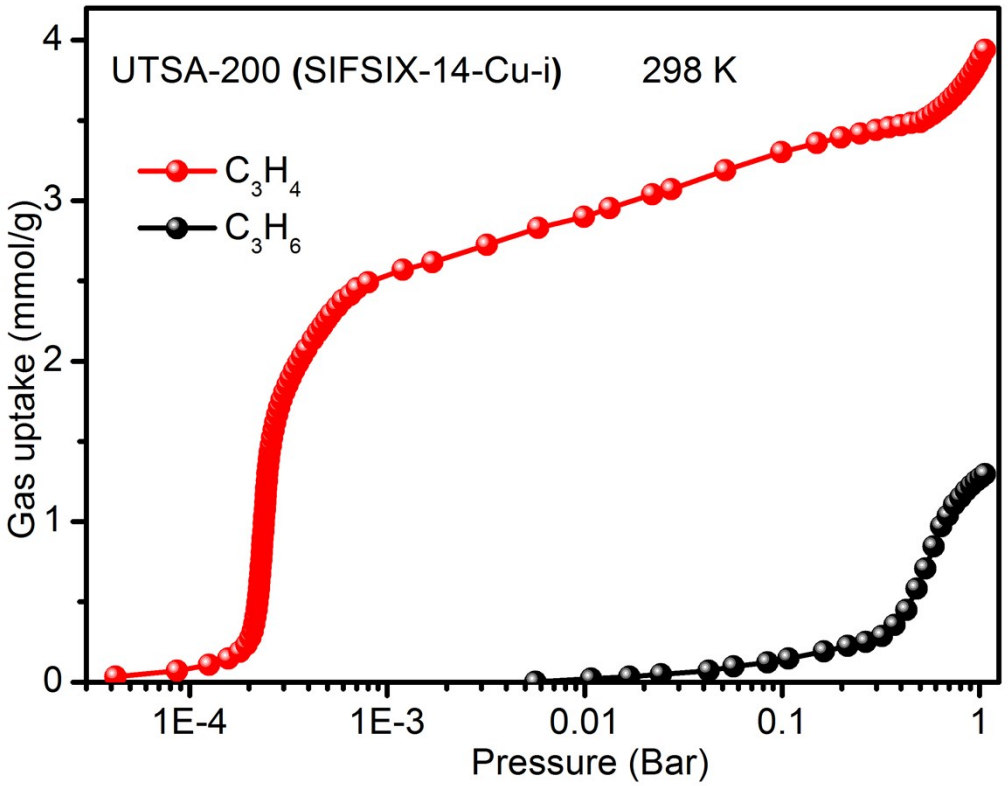

Fig. S20 The schematic of C_3H_4 and C_3H_6 gas adsorption isotherm for **UTSA-200 (SIFSIX-14-Cu-i)** at 298 K.

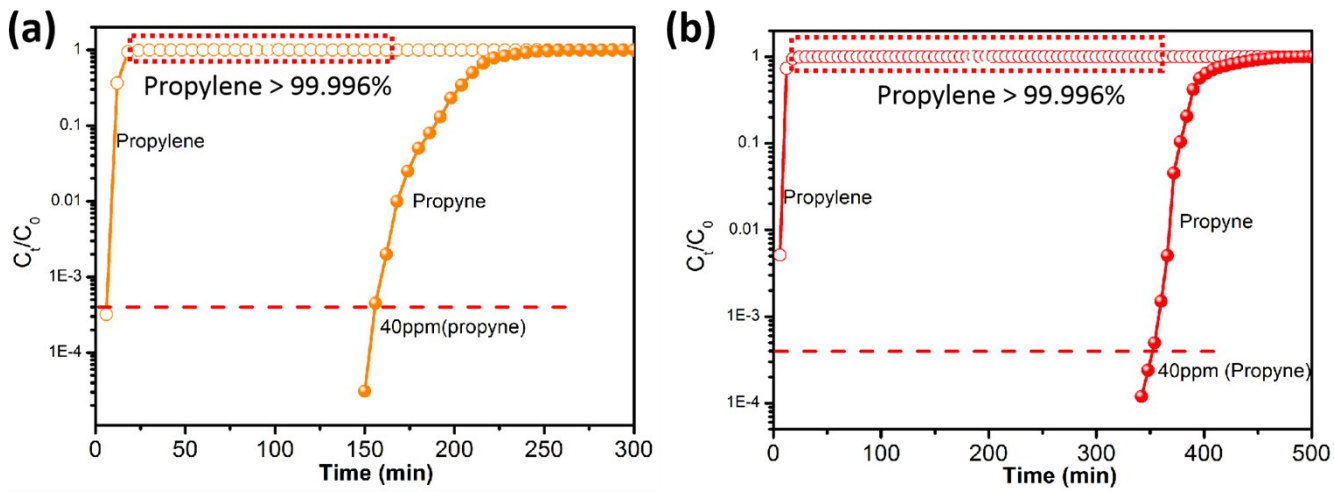

Fig. S21 (a) The concentrations of propylene in breakthrough experiments of **NKMOF-11** for propyne/propylene (1/99, v/v) and (b) for propyne/propylene (1/999, v/v).

Notation

b	Langmuir-Freundlich constant, $\mathrm{Pa}^{-\nu}$
q	component molar loading of species i, mol kg^{-1}
q_{sat}	saturation loading, mol kg^{-1}
L	length of packed bed adsorber, m
t	time, s
T	absolute temperature, K
u	superficial gas velocity in packed bed, m s^{-1}

Greek letters

ε	voidage of packed bed, dimensionless
ν	Freundlich exponent, dimensionless
ρ	crystal framework density, kg L^{-1}
τ	time, dimensionless

References

1 Y.-L. Peng, T. Pham, P. Li, T. Wang, Y. Chen, K.-J. Chen, K. A. Forrest, B. Space, P. Cheng, M. J. Zaworotko, Z. Zhang, *Angew. Chem. Int. Ed.* 2018, **57**, 10971-10975.

2 a) K.-J. Chen, Hayley S. Scott, David G. Madden, T. Pham, A. Kumar, A. Bajpai, M. Lusi, Katherine A. Forrest, B. Space, John J. Perry, Michael J. Zaworotko, *Chem* 2016, **1**, 753-765. b) x. Cui, K-J Chen, H. Xing, Q. Yang, R. Krishna, Z. Bao, H. Wu, W. Zhou, X. Dong, Y. Han, B Li, Q. Ren, M. J. Zaworotko, B. Chen, *Science* 2016, **353**, 141-144; c) L. Li, H.-M. Wen, C. He, R.-B. Lin, R. Krishna, H. Wu, W. Zhou, Ji. Li, B. Li, B. Chen, *Angew. Chem. Int. Ed.* 2018, **130**, 17.

3 R. T. Yang, *Gas separation by adsorption processes*, Butterworth-Heinemann, 1986.

4 H. Pan, J. A. Ritter, P. B. Balbuena, *Langmuir* 1998, **14**, 6323-6327.

5 U. W. F. S, *Journal of the Institute of Actuaries* 1924, **55**, 202-203.

6 J. E. Jones, S. Chapman, *Proceedings of the Royal Society of London. Series A, Containing Papers of a Mathematical and Physical Character* 1924, **106**, 463-477.

7 W. L. Jorgensen, D. S. Maxwell, J. Tirado-Rives, *J. Am. Chem. Soc.* 1996, **118**, 11225-11236.

8 A. K. Rappe, C. J. Casewit, K. S. Colwell, W. A. Goddard, W. M. Skiff, *J. Am. Chem. Soc.* 1992, **114**, 10024-10035.

9 a) P. C. Hariharan, J. A. Pople, *Theoretica chimica acta* 1973, **28**, 213-222; b) M. M. Francl, W. J. Pietro, W. J. Hehre, J. S. Binkley, M. S. Gordon, D. J. DeFrees, J. A. Pople, *The Journal of Chemical Physics* 1982, **77**, 3654-3665.

10 a) W. J. Stevens, H. Basch, M. Krauss, *The Journal of Chemical Physics* 1984, **81**, 6026-6033; b) P. J. Hay, W. R. Wadt, *The Journal of Chemical Physics* 1985, **82**, 270-283; c) L. A. LaJohn, P. A. Christiansen, R. B. Ross, T. Atashroo, W. C. Ermler, *The Journal of Chemical Physics* 1987, **87**, 2812-2824.

11 M. Valiev, E. J. Bylaska, N. Govind, K. Kowalski, T. P. Straatsma, H. J. J. Van Dam, D. Wang, J. Nieplocha, E. Apra, T. L. Windus, W. A. de Jong, *Comput. Phys. Commun.* 2010, **181**, 1477-1489.

12 (a) L. E. Chirlian, M. M. Francl, *J. Comput. Chem.* 1987, **8**, 894-905; (b) C. M. Breneman, K. B. Wiberg, *J. Comput. Chem.* 1990, **11**, 361-373.

13 P. T. van Duijnen, M. Swart, *The Journal of Physical Chemistry A* 1998, **102**, 2399-2407.

14 a) T. Pham, K. A. Forrest, R. Banerjee, G. Orcajo, J. Eckert, B. Space, *The Journal of Physical Chemistry C* 2015, **119**, 1078-1090; b) K. A. Forrest, T. Pham, K. McLaughlin, J. L. Belof, A. C. Stern, M. J. Zaworotko, B. Space, *The Journal of Physical Chemistry C* 2012, **116**, 15538-15549.

15 N. Metropolis, A. W. Rosenbluth, M. N. Rosenbluth, A. H. Teller, E. Teller, *The Journal of Chemical Physics* 1953, **21**, 1087-1092.

16 Y.-L. Peng, C. He, T. Pham, T. Wang, P. Li, R. Krishna, K. A. Forrest, A. Hogan, S. Suepaul, B. Space, M. Fang, Y. Chen, M. J. Zaworotko, J. Li, L. Li, Z. Zhang, P. Cheng, B. Chen, *Angew. Chem. Int. Ed.* 2019, **58**, 10209-10214.

17 B. A. Wells, A. L. Chaffee, *Journal of Chemical Theory and Computation* 2015, **11**, 3684-3695.

18 a) J. Applequist, J. R. Carl, K.-K. Fung, *J. Am. Chem. Soc.* 1972, **94**, 2952-2960; b) B. T. Thole, *Chem. Phys.* 1981, **59**, 341-350; c) K. A. Bode, J. Applequist, *The Journal of Physical Chemistry* 1996, **100**, 17820-17824; (d) K. McLaughlin, C. R. Cioce, T. Pham, J. L. Belof, B. Space, *The Journal of Chemical Physics* 2013, **139**, 184112.

[9 a) D. M. Franz, J. L. Belof, K. McLaughlin, C. R. Cioce, B. Tudor, A. Hogan, L. Laratelli, M. Mulcair, M. Mostrom, A. Navas, A. C. Stern, K. A. Forrest, T. Pham, B. Space, *Advanced Theory and Simulations* 2019, **2**, 1900113.

20 a) G. Kresse, J. Hafner, *Physical Review B* **1993**, *47*, 558-561; b) G. Kresse, J. Hafner, *Physical Review B* **1994**, *49*, 14251-14269; c) G. Kresse, J. Furthmüller, *Physical Review B* 1996, **54**, 11169-11186.

21 a) P. E. Blöchl, *Physical Review B* **1994**, *50*, 17953-17979; b) G. Kresse, D. Joubert, *Physical Review B* 1999, **59**, 1758-1775.

22 J. P. Perdew, K. Burke, M. Ernzerhof, *Phys. Rev. Lett.* 1996, **77**, 3865-3868.

23 S. Grimme, *J. Comput. Chem.* 2006, **27**, 1787-1799.

24 R. Krishna, *RSC Advances* 2017, **7**, 35724-35737.

25 R. Krishna, *Microporous Mesoporous Mater.* 2014, **185**, 30-50.

26 R. Krishna, *RSC Advances* 2015, **5**, 52269-52295.[27] R. Krishna, *Sep. Purif. Technol.* 2018, **194**, 281-300.